AIMS Mathematics, 11(6): 17880–17916.
DOI: 10.3934/math.2026729
Received: 19 March 2026
Revised: 10 May 2026
Accepted: 27 May 2026
Published: 18 June 2026

https://www.aimspress.com/journal/Math

Research article

Memory-based prey-taxis and environmental stress shape spatiotemporal predator-prey dynamics

Dazhuo Liu[1,*] **and Xuewen Tan**[2]

[1] College of Education and Psychology Science, Minnan Normal University, Zhangzhou Fujian 363000, China

[2] School of Mathematics and Computer Science, Yunnan Minzu University, Kunming 650504, China

* **Correspondence:** Email: ldz1834@mnnu.edu.cn.

Abstract: This paper investigates a diffusive predator–prey system incorporating memory-based prey-taxis, the Allee effect, and environmental stressors. After establishing global well-posedness and existence conditions for equilibria, we use prey-taxis sensitivity and memory delay as parameters to identify Turing and Hopf bifurcation thresholds. Our results show that strong memory-based prey-taxis suppresses diffusion-driven Turing patterns and restores spatial homogeneity. However, this spatial stabilization does not necessarily imply greater delay tolerance: The critical Hopf delay may decrease with taxis sensitivity, revealing a trade-off between taxis-induced spatial stabilization and delay-induced temporal oscillations. Additionally, we analyze environmental stress, revealing a predator release effect where moderate stress disproportionately suppresses predators, which indirectly leads to an increase in the prey's density. We also identify a mode-jumping phenomenon in the critical delay threshold during stress-induced transitions from ordinary differential equation (ODE) to Turing instability. Finally, the numerical simulations provide a two-parameter stability map delineating four dynamic regions: Stable homogeneous states, stationary Turing patterns, spatially nonhomogeneous periodic solutions, and complex spatiotemporal dynamics from interacting instabilities.

Keywords: predator–prey model; memory-based prey-taxis; environmental stress; spatiotemporal patterns; mathematical modeling ability
Mathematics Subject Classification: 92D25, 35B36

1. Introduction

The spatiotemporal dynamics of predator–prey interactions have long been a central theme in theoretical ecology and mathematical biology [1]. Classical models based on ordinary differential equations typically assume that populations are spatially homogeneous, an assumption that often fails to capture

the complex spatial patterns, such as patches, stripes, and waves, observed in real-world ecosystems. To address this limitation, reaction–diffusion systems have been extensively used to explore how the interplay between local reaction kinetics and random mobility drives the emergence of spatial heterogeneity through diffusion-driven instability, commonly known as Turing instability [2–4]. These models have successfully demonstrated that spatial diffusion can destabilize a uniform equilibrium, leading to the formation of rich spatiotemporal patterns [5–10].

While random diffusion characterizes nondirectional movement, predators in realistic ecosystems exhibit directed movements driven by sensory perception, commonly known as taxis. A substantial body of literature has investigated predator–prey models with prey-taxis, where predators move up the gradient of prey density [11–16]. However, most existing models assume that predators respond instantaneously to the current environment. Recent biological and mathematical studies suggest that higher-level organisms rely on cognitive maps—internal representations of the environment based on past experiences—to guide their foraging [17, 18]. This introduces a memory effect, implying that the predator's movement depends on the prey's distribution at a past time. Such memory-based diffusion effectively introduces a time delay into the spatial movement term, which has been shown to significantly alter the boundaries of stability and induce complex bifurcation phenomena, such as spatially inhomogeneous Hopf bifurcations [19–23].

In addition to intrinsic behavioral mechanisms, ecosystems are increasingly threatened by external anthropogenic disturbances, particularly environmental pollution and toxins. The presence of environmental stressors imposes additional mortality rates and can fundamentally shift ecological balances by triggering abrupt regime shifts once the critical thresholds are crossed [24, 25]. A recent study by Thommandru and Kundu highlighted that stress-driven responses can uncover ecological tipping points, where even small environmental perturbations may lead to irreversible shifts in population dynamics, such as the transition from stable coexistence to extinction [26]. The impact of toxins on population dynamics is complex; for instance, toxins can alter competitive outcomes [27] or dictate species' persistence in polluted environments [28, 29]. Furthermore, many species exhibit the Allee effect at low population densities, where individual fitness correlates positively with the population size [30, 31]. The combined effect of environmental toxicity and the Allee effect can drive catastrophic transitions [32]. However, while the individual effects of cognitive movement and environmental stress have been studied, the specific interaction between memory-driven movement (internal mechanism) and environmental stress (external pressure) remains largely unexplored, particularly regarding how cognitive maps might mitigate or exacerbate stress-induced instabilities.

Motivated by the complex interplay between internal cognitive processes and external environmental disturbances, this paper proposes a diffusive predator–prey model that integrates memory-based prey-taxis, the Allee effect, and environmental stress. To mathematically formulate these mechanisms, we consider the following reaction–diffusion–advection system:

$$\begin{cases} u_t = d_1\Delta u + ru(1-\frac{u}{K}) - \frac{\alpha uv}{u+mv} - \beta_1 u\eta, & x\in\Omega, \quad t>0,\\ v_t = d_2\Delta v - \chi\nabla\cdot(v\nabla u(x,t-\tau)) + \frac{\beta uv}{u+mv} - \gamma v - \beta_2 v(A-u) - \beta_3 v\eta - \gamma_1 v^2, & x\in\Omega, \quad t>0,\\ \frac{\partial u}{\partial n} = \frac{\partial v}{\partial n} = 0, & x\in\partial\Omega, \quad t>0,\\ u(x,t) = u_0(x,t), & x\in\Omega, t\in[-\tau,0],\\ v(x,0) = v_0(x), & x\in\Omega, \end{cases} \tag{1.1}$$

where $u(x,t)$ and $v(x,t)$ denote the densities of the resource (prey) and consumer (predator) populations at location x and time t, respectively. The spatial domain $\Omega\subset\mathbb{R}^n(n=1,2,3)$ is a bounded region with

a smooth boundary $\partial\Omega$. The parameters $d_1, d_2 > 0$ are the diffusion coefficients for the resource and consumer, respectively. The term $\chi > 0$ represents the strength of memory-based prey-taxis, with $\tau \geq 0$ being the time delay reflecting the cognitive memory effect. The remaining parameters $(r, K, \alpha, m, \beta, \gamma, \beta_1, \beta_2, \beta_3, A, \gamma_1)$ are all positive constants characterizing various biological interactions and environmental effects.

Predation is described by the ratio-dependent functional response $\frac{\alpha uv}{u+mv}$. Equivalently, the per capita predation rate is $\frac{\alpha u}{u+mv} = \frac{\alpha(u/v)}{u/v+m}$, which depends on the prey-to-predator ratio u/v. This formulation reflects the fact that predator interference or competition among predators can reduce the effective predation rate when predator density is high. Here, α denotes the maximum predation rate, and m measures the strength of predator interference in the ratio-dependent response. Finally, the term $\beta_1 u\eta$ incorporates mortality due to an external environmental stressor, such as a toxin or habitat degradation, where η is the stressor's intensity and β_1 is the associated sensitivity coefficient.

The equation governing the consumer's dynamics v is more complex. A central feature of this model is the memory-based prey-taxis term, $-\chi\nabla \cdot (v\nabla u(x, t-\tau))$, which posits that the consumer's movement is directed along the resource density gradient from a past time $t-\tau$. The parameter $\chi > 0$ measures the taxis sensitivity, and $\tau \geq 0$ is the memory period or time delay. The growth of the consumer population is driven by predation, captured by $\frac{\beta uv}{u+mv}$, with β being the biomass conversion efficiency. The consumer faces several demographic pressures. Besides natural mortality at rate γ, we include the term $-\beta_2 v(A-u)$, which represents a resource-mediated Allee-type effect on the predator population. This term is not a classical Allee effect determined by the predator density itself. Rather, it describes an indirect demographic limitation caused by insufficient prey availability. Indeed, its per capita contribution is $-\beta_2(A-u)$. Hence, when the prey density is below the threshold A, i.e., $u < A$, the predator experiences an additional negative growth pressure due to prey scarcity; when $u > A$, this pressure is relaxed and the predator population benefits from adequate prey supply. In this sense, A denotes the critical prey density required for predators' persistence, and β_2 measures the intensity of this prey-threshold-induced effect. This structure is consistent with recent predator–prey models with environmental stress, where the predators' survival is assumed to depend critically on prey availability. The term $-\beta_3 v\eta$ accounts for the direct negative impact of the environmental stressor on the predator, while $-\gamma_1 v^2$ describes intraspecific competition among predators.

The system evolves within a closed environment, as enforced by the zero-flux Neumann boundary conditions, $\frac{\partial u}{\partial n} = \frac{\partial v}{\partial n} = 0$, on the boundary $\partial\Omega$. The biological interpretations of the parameters are summarized in Table 1.

We assume that the initial conditions satisfy the following regularity and non-negativity assumptions.

(H_1) The initial functions satisfy

$$u_0 \in C([-\tau, 0]; W^{1,p}(\Omega)) \quad \text{and} \quad v_0 \in W^{1,p}(\Omega),$$

for some $p > n$. Furthermore, the initial data are non-negative

$$u_0(x,t) \geq 0 \quad \text{for all } (x,t) \in \bar{\Omega} \times [-\tau, 0], \quad v_0(x) \geq 0 \quad \text{for all } x \in \bar{\Omega}.$$

Our primary objective is to understand how the predator's cognitive delay and environmental harshness collectively shape the ecosystem's resilience and spatiotemporal organization. Through analytical investigation and numerical verification, this study provides the following main insights.

Table 1. Biological/ecological meaning of the parameters.

Parameters	Biological/ecological meaning
r	Intrinsic growth rate of the prey population
K	Environmental carrying capacity for the prey population
α	Maximum predation rate of the predator on the prey
m	Predator interference coefficient in the ratio-dependent functional response
β	Conversion efficiency of prey into predator biomass
γ	Natural death rate of the predator
γ_1	Intraspecific competition coefficient for the predator population
τ	Time delay or memory period for the predator's taxis response
$d_i (i = 1, 2)$	Random diffusion coefficients for the prey and predator, respectively
χ	Memory-based prey-taxis coefficient
η	Intensity of external environmental stress (or toxin)
β_1	Stress impact coefficient on the prey population
β_2	Strength of the prey-threshold-induced Allee-type effect on the predator population
β_3	Stress impact coefficient on the predator population
A	Critical prey density required for predators' persistence

(i) We identify a nontrivial role of attractive prey-taxis in shaping spatiotemporal stability. In the absence of a large delay, strong memory-based prey-taxis can suppress diffusion-driven Turing patterns and restore spatial homogeneity. However, this stabilizing effect on spatial patterns is accompanied by increased sensitivity to delayed feedback: The critical Hopf delay may decrease as the taxis sensitivity increases. Thus, prey-taxis produces a trade-off between spatial stabilization and temporal delay-induced instability.

(ii) We reveal a counterintuitive predator release effect driven by environmental stress. Our analysis shows that moderate stress levels can suppress the predator population more severely than the prey, leading to a paradoxical increase in prey density and a shift in the community structure.

(iii) We uncover the phenomenon of mode jumping in the critical delay threshold and construct a comprehensive two-parameter stability map. This map delineates distinct dynamic regions, identifying a codimension-2 bifurcation point where spatial (Turing) and temporal (Hopf) instabilities interact to generate complex spatiotemporal dynamics.

The remainder of this paper is organized as follows. In Section 2, we establish the mathematical well-posedness of the proposed model by proving the global existence and uniform boundedness of non-negative solutions. Section 3 provides a detailed analysis of the existence conditions for both boundary and coexistence equilibria. In Section 4, we perform a comprehensive stability and bifurcation analysis. In Section 5, we derive the normal form of the Hopf bifurcation induced by the cognitive delay, characterizing the stability and direction of the bifurcating periodic solutions. Section 6 presents extensive numerical simulations to verify the theoretical results, illustrating the dual stabilizing role of taxis, the emergence of spatiotemporal patterns, and the complex impacts of environmental stress. Finally, the paper concludes with a summary of the main findings and their ecological implications in Section 7.

2. Global existence and boundedness

This section focuses on the global existence and boundedness of solutions for Model (1.1). We begin by presenting the existence of solutions as outlined in the following lemma.

Lemma 2.1. *Assume that the initial conditions satisfy* (H_1)*. We then have*

(i) System (1.1) *has a unique solution* $(u(x,t), v(x,t)) \in \overline{\Omega} \times (0,\infty)$*, which is positive and satisfies*

$$(u(x,t), v(x,t)) \in \left[W_p^{2,1} \cap C^{2+\theta,1+\frac{\theta}{2}}\left(\bar{\Omega} \times (0,\infty)\right)\right]^2.$$

Moreover, if the initial function satisfies $u_0(x,t) \gneqq 0$, $v_0(x) \gneqq 0$, *then* $u(x,t) > 0$, $v(x,t) > 0$ *for* $x \in \Omega$ *and* $t > 0$.

(ii) $M_1 > 0$ *exists such that*

$$u(x,t) \leq M_1, \quad for \quad x \in \bar{\Omega}, t \in [-\tau,\infty).$$

(iii) $C_u > 0$ *and* $C_v > 0$ *exist such that*

$$\int_\Omega u(x,t)dx \leq C_u, \int_\Omega v(x,t)dx \leq C_v.$$

Proof. (i) For $t \in [0,\tau]$, u_τ coincides with the initial function $u_0(x,t)$. Let

$$\begin{aligned} F_1(t,x,u,v) &= ru(1-\frac{u}{K}) - \frac{\alpha uv}{u+mv} - \beta_1 u\eta, \\ F_2(t,x,u,v) &= -\chi\nabla\cdot(v\nabla u_0(x,t-\tau)) + \frac{\beta uv}{u+mv} - \gamma v - \beta_2 v(A-u) - \beta_3 v\eta - \gamma_1 v^2, \end{aligned} \tag{2.1}$$

It is clear that F_1 and F_2 are continuous, satisfying a Hölder condition with respect to t and a Lipschitz condition with respect to u and v.

Since $\partial\Omega$ is C^2, according to [33], Proposition 7.3.3, there is a unique solution for $u(x,t)$, $v(x,t)$ on $[0,\delta]$ for some $\delta > 0$. Moreover, $u(x,t)$ and $v(x,t)$ can be extended to $[0,\tau]$. It is noted that $v(x,t)$ satisfies

$$\begin{cases} \dfrac{\partial v}{\partial t} \leq d_2\Delta v - \chi\nabla\cdot(v\nabla u_0(x,t-\tau)) + \beta v, & x \in \Omega, t > 0, \\ \dfrac{\partial v}{\partial \mathbf{n}} = 0, & x \in \partial\Omega, t > 0, \\ v(x,0) = v_0(x), & x \in \Omega. \end{cases} \tag{2.2}$$

Then $v(x,t)$ can similarly be extended to $[0,\tau]$. By repeating this process, the solution can be extended to $[\tau,2\tau]$ and subsequently to $[k\tau,(k+1)\tau]$ for any $k \in \mathbb{N}$. Furthermore, by applying the maximum principle, we have $u(x,t) > 0$, $v(x,t) > 0$ for all $(x,t) \in [0,\infty)$.

(ii) From the first equation of System (1.1), we get

$$\begin{cases} \dfrac{\partial u}{\partial t} = d_1\Delta u + ru(1-\dfrac{u}{K}) - \dfrac{\alpha uv}{u+mv} - \beta_1 u\eta \leq ru(1-\dfrac{u}{K}), & (x,t) \in \Omega \times (0,+\infty), \\ \dfrac{\partial u}{\partial \mathbf{n}} = 0, & x \in \partial\Omega, \\ u(x,t) = u_0(x,t) \leq \max_{t\in[-\tau,0]}\{u(x,t)\}, & x \in \Omega, t \in [-\tau,0]. \end{cases}$$

Using the comparison principle, a constant $C_1 > 0$ exists such that

$$\sup_{0\le t\le\infty} \left\|u(x,t)\right\|_{L^\infty} \le \max\left\{K, \max_{t\in[-\tau,0]} \left\|u_0(\cdot,t)\right\|_{L^\infty}\right\} := M_1. \tag{2.3}$$

(iii) Integrating the first equation of System (1.1) over Ω gives

$$\frac{d}{dt}\int_\Omega u\,dx = \int_\Omega \left[ru\left(1-\frac{u}{K}\right) - \frac{\alpha uv}{u+mv} - \beta_1 u\eta\right]dx \le \int_\Omega ru\left(1-\frac{u}{K}\right)dx.$$

Using Hölder's inequality, $\int_\Omega u^2 dx \ge \frac{1}{|\Omega|}\left(\int_\Omega u dx\right)^2$, we obtain

$$\frac{d}{dt}\int_\Omega u\,dx \le r\int_\Omega u\,dx - \frac{r}{K|\Omega|}\left(\int_\Omega u\,dx\right)^2.$$

This logistic-type inequality implies $\int_\Omega u dx \le C_u$ for some $C_u > 0$.

Integrating the second equation of System (1.1) over Ω yields

$$\begin{aligned}
\frac{d}{dt}\int_\Omega v\,dx &= \int_\Omega \left[\frac{\beta uv}{u+mv} - \gamma v - \beta_2 v(A-u) - \beta_3 v\eta - \gamma_1 v^2\right]dx \\
&\le \int_\Omega \left[\beta v - \gamma v - \beta_2 Av + \beta_2 M_1 v - \beta_3\eta v - \gamma_1 v^2\right]dx \quad (\text{since } u \le M_1) \\
&= \int_\Omega \left[C_1 v - \gamma_1 v^2\right]dx,
\end{aligned}$$

where $C_1 = \beta - \gamma - \beta_2 A + \beta_2 M_1 - \beta_3\eta$. Again, by Hölder's inequality,

$$\frac{d}{dt}\int_\Omega v\,dx \le C_1\int_\Omega v\,dx - \frac{\gamma_1}{|\Omega|}\left(\int_\Omega v\,dx\right)^2,$$

so $\int_\Omega v dx \le C_v$ for some $C_v > 0$.

□

Next we recall some preliminary estimates which will be used in our proof.

Lemma 2.2. *[34] Let $(e^{t\Delta})$ represents the Neumann heat semigroup in Ω, and let $\mu_1 > 0$ denote the first nonzero eigenvalue of $-\Delta$ in Ω under homogeneous Neumann boundary conditions. Then, for all $t > 0$, there are constants $\xi_i(\Omega)(i = 1, 2, 3, 4)$ that depend on Ω and satisfy the following properties.*

(i) For $1 \le q \le p \le \infty$ and any $w \in L^q(U)$ satisfying $\int_U w = 0$, the following estimate holds

$$\|e^{td\Delta}w\|_{L^p(U)} \le \xi_1\left(1 + t^{-\frac{n}{2}(\frac{1}{q}-\frac{1}{p})}\right)e^{-d\lambda_1 t}\|w\|_{L^q(U)}, \quad \text{for all } t > 0. \tag{2.4}$$

(ii) For $1 \le q \le p \le \infty$ and any $w \in L^q(U)$, the gradient of the solution satisfies

$$\|\nabla e^{td\Delta}w\|_{L^p(U)} \le \xi_2\left(1 + t^{-\frac{1}{2}-\frac{n}{2}(\frac{1}{q}-\frac{1}{p})}\right)e^{-d\lambda_1 t}\|w\|_{L^q(U)}, \quad \text{for all } t > 0. \tag{2.5}$$

(iii) For $2 \le p < \infty$ and any $w \in W^{1,p}(U)$, the gradient of the solution satisfies

$$\|\nabla e^{td\Delta}w\|_{L^p(U)} \le \xi_3 e^{-d\lambda_1 t}\|\nabla w\|_{L^p(U)}, \quad \text{for all } t > 0. \tag{2.6}$$

(iv) For $1 < q \le p < \infty$ and any $w \in (C_0^\infty(U))^n$, the divergence of the solution satisfies

$$\|e^{td\Delta}(\nabla \cdot w)\|_{L^p(U)} \le \xi_4 \left(1 + t^{-\frac{1}{2}-\frac{n}{2}(\frac{1}{q}-\frac{1}{p})}\right) e^{-d\lambda_1 t}\|w\|_{L^q(U)}, \quad \text{for all } t > 0. \tag{2.7}$$

Moreover, the operator $e^{t\Delta}\nabla\cdot$ admits a unique extension to an operator from $L^q(U)$ to $L^p(U)$, with its norm controlled by (2.7).

Lemma 2.3. *[34] Suppose that $z(t)$ satisfies*

$$\begin{cases} z'(t) \le -az^b(t) + cz(t) + d, \\ z(0) = z_0 > 0, \end{cases}$$

where $a > 0$, $c > 0$, $d > 0$, and $b > 1$. Then

$$z(t) \le \max\{C(z_0), C(a, c, d)\}.$$

Lemma 2.4. *[35] Assume that $i, j \ge 1$ satisfy $i(N - j) < jN$ and $m \in (0, i)$. Then there is a positive constant C such that for any $u \in W^{1,j}(\Omega)$, the following inequality holds:*

$$\|u\|_{L^i(\Omega)} \le C_5\|u\|^{\kappa}_{W^{1,j}(\Omega)}\|u\|^{1-\kappa}_{L^m(\Omega)},$$

where κ is defined by

$$\kappa = \frac{\frac{N}{m} - \frac{N}{i}}{\frac{N}{m} + 1 - \frac{N}{j}} \in (0, 1).$$

Lemma 2.5. *[35] Suppose that $i > 1$ and $j > 0$. Then a positive C exists such that for any $u \in W^{1,j}(\Omega)$ fulfilling*

$$\left\|u\right\|_{W^{1,j}(\Omega)} \le C\left(\left\|\nabla u\right\|_{L^i(\Omega)} + \left\|u\right\|_{L^j}(\Omega)\right).$$

Lemma 2.6. *Consider $\Omega \subset \mathbb{R}^n (n \ge 1)$, a bounded domain with a smooth boundary, and let (u, v) represents the solution to System* (1.1)*. For any initial conditions that satisfy (H_1), we have*

$$\|v(\cdot, t)\|_{L^p(\Omega)} \le M_2, \quad \forall t \in (0, \infty).$$

Proof. For notational convenience, throughout the following estimates, we write

$$u_\tau(x, t) := u(x, t - \tau).$$

In particular,

$$\nabla u_\tau(x, t) = \nabla u(x, t - \tau), \qquad \Delta u_\tau(x, t) = \Delta u(x, t - \tau).$$

We first show that for any $0 < \varepsilon < 1$, a constant $C(\varepsilon) > 0$ exists such that

$$\|u(\cdot, t)\|_{1,\infty} \le C(\varepsilon), \quad t \in (\varepsilon, \infty).$$

The first equation of (1.1) can be rewritten as

$$u_t = d_1\Delta u - u + F_1(x, t), \tag{2.8}$$

where $F_1(x,t) = ru(1-\frac{u}{K}) - \frac{\alpha uv}{u+mv} - \beta_1 u\eta + u$. By (2.3), we then have

$$\begin{aligned}\|F_1(\cdot,t)\|_{L^q} =& \Big\| ru(1-\frac{u}{K}) - \frac{\alpha uv}{u+mv} - \beta_1 u\eta + u \Big\|_{L^q} \\ \leq& M_1\Big(r + \frac{rM_1}{K} + \frac{\alpha}{m} + \beta_1\eta + 1\Big)|\Omega|^{\frac{1}{q}} := C_1.\end{aligned}$$

Applying ∇ to both sides of Equation (2.8), utilizing $L^p - L^q$ estimates, and choosing $q > n$ and $\theta \in \left(\frac{1}{2}\left(1+\frac{n}{q}\right), 1\right)$, we have

$$\begin{aligned}\|\nabla u(\cdot,t)\|_{L^\infty} &\leq \int_0^t \|\nabla e^{(t-\xi)(d_1\Delta-1)} F_1(\cdot,\xi)\|_{L^\infty} d\xi + \|\nabla e^{(d_1\Delta-1)t} u_0\|_{L^\infty} \\ &\leq \xi_1 \|u_0\|_{W^{1,\infty}} + \int_0^t \|\nabla e^{(t-\xi)d_1\Delta} F_1(\cdot,\xi)\|_{L^\infty} d\xi \\ &\leq \xi_1 \|u_0\|_{W^{1,\infty}} + \xi_2 \int_0^t \left((t-\xi)^{-\theta} + 1\right) e^{-\mu_1 d_1 (t-\xi)} \|F_1(\cdot,\xi)\|_{L^q} d\xi \\ &\leq \xi_1 \|u_0\|_{W^{1,\infty}} + \xi_2 C_1 \int_0^\infty (1+z^{-\theta}) e^{-\mu_1 d_1 z} dz \\ &\leq \xi_1 \|u_0\|_{W^{1,\infty}} + \frac{\xi_2 C_1}{d_1\mu_1}\left(1 + \Gamma(1-\theta)(d_1\mu_1)^\theta\right),\end{aligned}$$

for all $t \in (\epsilon, \infty)$, where $\Gamma(1-\theta) > 0$ as $\theta < 1$ and C_2 is a positive constant depending on ξ_1, ξ_2, M_1, $\max_{t\in[\varepsilon,T]} \|u(\cdot,t)\|_q$.

Let

$$\widetilde{C_1} = \max\left\{C(\epsilon), \max_{t\in[-\tau,0]} \|\nabla u(\cdot,t)\|_\infty, \max_{t\in[0,1], x\in\overline{\Omega}} \{\|\nabla u(x,t)\|\}\right\}.$$

Then

$$\|\nabla u(\cdot,t)\|_\infty \leq \widetilde{C_1} \quad \text{on} \quad \Omega \quad \text{for all} \quad t \in [-\tau, \infty). \tag{2.9}$$

Thus, we have

$$\Big\|\nabla u(\cdot,t)\Big\|_{L^\infty} \leq C_3. \tag{2.10}$$

For every $p \geq 2$, consider the second equation in System (1.1). By multiplying each term of this

equation by kv^{k-1} and integrating the result across the domain Ω, we obtain

$$\begin{aligned}\frac{d}{dt}\int_\Omega v^k dx =& k\int_\Omega v^{k-1}v_t\\ =& kd_2\int_\Omega v^{k-1}\Delta v dx - \chi k\int_\Omega v^{k-1}\nabla\cdot(v\nabla u_\tau)dx\\ &+ k\int_\Omega v^{k-1}\Big(\frac{\beta uv}{u+mv} - \gamma v - \beta_2 v(A-u) - \beta_3 v\eta - \gamma_1 v^2\Big)dx\\ \le& -kd_2(k-1)\int_\Omega v^{k-2}|\nabla v|^2 dx - k(k-1)\chi\int_\Omega v^{k-1}\nabla v\cdot\nabla u_\tau dx\\ &+ k\int_\Omega v^{k-1}\Big(\beta v + \beta_2 uv - \gamma_1 v^2\Big)dx\\ \le& -\frac{4d_2(k-1)}{k}\int_\Omega |\nabla v^{\frac{k}{2}}|^2 dx + k(k-1)\chi C_3\int_\Omega v^{k-1}|\nabla v|dx\\ &+ k(\beta+\beta_2 M_1)\int_\Omega v^k dx - k\gamma_1\int_\Omega v^{k+1}dx,\end{aligned} \tag{2.11}$$

where we have used $u \le M_1$ from Theorem 2.1 to estimate $\beta_2 uv \le \beta_2 M_1 v$ and the bound $\|\nabla u_\tau\|_\infty \le C_3$.

Now, applying Young's inequality to the chemotaxis term with $\epsilon = \frac{2d_2}{k\chi C_3}$ and using the identity $v^{k-1}|\nabla v| = \frac{2}{k}v^{\frac{k}{2}}|\nabla v^{\frac{k}{2}}|$, we have

$$\begin{aligned}k(k-1)\chi C_3\int_\Omega v^{k-1}|\nabla v|dx &= 2(k-1)\chi C_3\int_\Omega v^{\frac{k}{2}}|\nabla v^{\frac{k}{2}}|dx\\ &\le \frac{2d_2(k-1)}{k}\int_\Omega |\nabla v^{\frac{k}{2}}|^2 dx + \frac{k(k-1)\chi^2 C_3^2}{2d_2}\int_\Omega v^k dx.\end{aligned}$$

Substituting this back into (2.11), we obtain

$$\frac{d}{dt}\int_\Omega v^k dx \le -\frac{2d_2(k-1)}{k}\int_\Omega |\nabla v^{\frac{k}{2}}|^2 dx + C_{coef}\int_\Omega v^k dx - k\gamma_1\int_\Omega v^{k+1}dx, \tag{2.12}$$

where $C_{coef} = \frac{k(k-1)\chi^2 C_3^2}{2d_2} + k(\beta+\beta_2 M_1)$. Since $-k\gamma_1\int_\Omega v^{k+1}dx \le 0$, we can drop it for the differential inequality derivation or keep it to strengthen the bound, but the gradient term suffices via the Gagliardo–Nirenberg inequality.

By Theorem 2.4 and Theorem 2.5, we have

$$\begin{aligned}\int_\Omega v^k dx =& \left\|v^{\frac{k}{2}}\right\|_2^2 \le C_5\left\|v^{\frac{k}{2}}\right\|_{W^{1,2}}^{2\vartheta}\left\|v^{\frac{k}{2}}\right\|_{L^{\frac{2}{k}}}^{2(1-\vartheta)}\\ \le& C_5C_6\left(\left\|\nabla v^{\frac{k}{2}}\right\|_{L^2} + \left\|v^{\frac{k}{2}}\right\|_{L^{\frac{2}{k}}}\right)^{2\vartheta}\left\|v^{\frac{k}{2}}\right\|_{L^{\frac{2}{k}}}^{2(1-\vartheta)}\\ =& C_5C_6\left(\left\|\nabla v^{\frac{k}{2}}\right\|_{L^2} + \left\|v\right\|_{L^1}^{\frac{k}{2}}\right)^{2\vartheta}\left\|v^k\right\|_{L^1}^{k(1-\vartheta)}\\ \le& C_7\left(\left\|\nabla v^{\frac{k}{2}}\right\|_{L^2} + 1\right)^{2\vartheta},\end{aligned} \tag{2.13}$$

where we utilize the uniform L^1 bound of v from Theorem 2.1, and choose

$$\vartheta = \frac{\frac{kn}{2} - \frac{n}{2}}{\frac{kn}{2} + 1 - \frac{n}{2}} = \frac{k-1}{k-1+\frac{2}{n}} \in (0,1).$$

From (2.13), we imply that

$$\int_\Omega |\nabla v^{\frac{k}{2}}|^2 = \|\nabla v^{\frac{k}{2}}\|_{L^2}^2 \geq C_8 \left(\int_\Omega v^k dx\right)^{\frac{1}{\vartheta}} - 1, \tag{2.14}$$

for some positive constant C_8. Combining (2.12) with (2.14) gives us

$$\frac{d}{dt}\int_\Omega v^k dx \leq -\frac{2d_2(k-1)C_8}{k}\left(\int_\Omega v^k dx\right)^{\frac{1}{\vartheta}} + C_{coef}\int_\Omega v^k dx + \frac{2d_2(k-1)}{k}.$$

Since $\frac{1}{\vartheta} = 1 + \frac{2}{n(k-1)} > 1$, the term $-\left(\int v^k\right)^{\frac{1}{\vartheta}}$ dominates the linear term $\int v^k$ for large values. On the basis of Theorem 2.3, we conclude that there is a positive constant C_9 such that

$$\left\|v(\cdot,t)\right\|_{L^k} \leq C_9, \quad t \in (0, T_{\max}).$$

□

Lemma 2.7. *Suppose that* (u, v) *is the solution to System* (1.1)*, and the conditions of Lemma 2.1 hold. A positive constant* C_{10} *exists such that*

$$\|v(\cdot,t)\|_{L^\infty(\Omega)} \leq C_{10}, \quad \textit{for all } t \in (0,\infty). \tag{2.15}$$

Proof. We rewrite the second equation of (1.1) as follows:

$$v_t - d_2\Delta v + v = -\chi\nabla\cdot(v\nabla u_\tau) + g(x,t), \tag{2.16}$$

where

$$g(x,t) = \frac{\beta uv}{u+mv} - \gamma v - \beta_2 v(A-u) - \beta_3 v\eta - \gamma_1 v^2 + v.$$

Utilizing the variation of constants formula, we have

$$\begin{aligned} v(\cdot,t) = e^{t(d_2\Delta-1)}v_0 - \chi\int_0^t e^{(t-\xi)(d_2\Delta-1)}\nabla\cdot(v(\cdot,\xi)\nabla u(\cdot,\xi-\tau))d\xi \\ + \int_0^t e^{(t-\xi)(d_2\Delta-1)}g(\cdot,\xi)d\xi. \end{aligned} \tag{2.17}$$

From Lemma 2.1, we know that $u \leq M_1$. Furthermore, noting that $-\gamma_1 v^2 \leq 0$ and dropping the nonpositive terms, we can estimate $g(x,t)$ linearly with respect to v

$$g(x,t) \leq (\beta + \beta_2 M_1 + 1)\, v(x,t) := C_{coef} v(x,t).$$

Moreover, from (2.10), we have the uniform boundedness of the prey gradient $\|\nabla u(\cdot, t-\tau)\|_{L^\infty} \leq C_3$.

We now fix $q > n$. According to Lemma 2.6, $C_q > 0$ exists such that $\|v(\cdot,t)\|_{L^q} \leq C_q$ for all $t > 0$.

We estimate the terms in (2.17) using the smoothing properties of the Neumann heat semigroup given in Lemma 2.2.

Using the maximum principle (or (2.4) with $p = q = \infty$), we have

$$\|e^{t(d_2\Delta-1)}v_0\|_{L^\infty} \leq e^{-t}\|v_0\|_{L^\infty} \leq \|v_0\|_{L^\infty}. \tag{2.18}$$

Using Estimate (2.4) from Lemma 2.2 with $p = \infty$, we obtain

$$\begin{aligned}\left\|\int_0^t e^{(t-\xi)(d_2\Delta-1)}g(\cdot,\xi)d\xi\right\|_{L^\infty} &\leq \int_0^t \left\|e^{(t-\xi)(d_2\Delta-1)}g(\cdot,\xi)\right\|_{L^\infty} d\xi \\ &\leq C_{coef}\xi_1 \int_0^t \left(1+(t-\xi)^{-\frac{n}{2q}}\right)e^{-(t-\xi)}\|v(\cdot,\xi)\|_{L^q}d\xi \\ &\leq C_{coef}\xi_1 C_q \int_0^\infty \left(1+s^{-\frac{n}{2q}}\right)e^{-s}ds.\end{aligned} \tag{2.19}$$

Since $q > n$, we have $\frac{n}{2q} < \frac{1}{2} < 1$, so the integral converges to a constant (involving the Gamma function).

Using Estimate (2.7) from Lemma 2.2 with $p = \infty$, we obtain

$$\begin{aligned}&\left\|\chi\int_0^t e^{(t-\xi)(d_2\Delta-1)}\nabla\cdot(v(\cdot,\xi)\nabla u(\cdot,\xi-\tau))d\xi\right\|_{L^\infty} \\ &\leq \chi\xi_4\int_0^t\left(1+(t-\xi)^{-\frac{1}{2}-\frac{n}{2q}}\right)e^{-(t-\xi)}\|v(\cdot,\xi)\nabla u(\cdot,\xi-\tau)\|_{L^q}d\xi \\ &\leq \chi\xi_4\int_0^t\left(1+(t-\xi)^{-\frac{1}{2}-\frac{n}{2q}}\right)e^{-(t-\xi)}\|v(\cdot,\xi)\|_{L^q}\|\nabla u(\cdot,\xi-\tau)\|_{L^\infty}d\xi \\ &\leq \chi\xi_4 C_q C_3\int_0^\infty\left(1+s^{-\frac{1}{2}-\frac{n}{2q}}\right)e^{-s}ds.\end{aligned} \tag{2.20}$$

Since $q > n$, we have $\frac{1}{2}+\frac{n}{2q} < 1$, ensuring the integral converges.

Combining (2.18), (2.19), and (2.20), we conclude that there is a constant $C_{10} > 0$ independent of t such that

$$\|v(\cdot,t)\|_{L^\infty} \leq C_{10}, \quad \text{for all } t \in (0,\infty).$$

□

According to lemma 2.1 and lemma 2.7, we can obtain the boundedness of solutions for the system (1.1) as follows.

Theorem 2.8. *Assume that the initial conditions satisfy* (H_1)*. Then System* (1.1) *has a unique solution* $(u(x,t),v(x,t)) \in \left[W_p^{2,1}\cap C^{2+\theta,1+\frac{\theta}{2}}\left(\bar{\Omega}\times(0,\infty)\right)\right]^2$*. Moreover, for* $p > n$*, a constant* $M > 0$ *exists such that*

$$\|u(\cdot,t)\|_{W^{1,\infty}(\Omega)} + \|v(\cdot,t)\|_{L^\infty(\Omega)} \leq M, \ \ for\ t \in [-\tau,\infty).$$

3. Existence of equilibria

In this section, we analyze the existence of spatially homogeneous equilibria of System (1.1). The constant solutions (u,v) satisfy the following algebraic system:

$$\begin{cases} u\left[r\left(1-\frac{u}{K}\right)-\frac{\alpha v}{u+mv}-\beta_1\eta\right]=0, \\ v\left[\frac{\beta u}{u+mv}-\gamma-\beta_2(A-u)-\beta_3\eta-\gamma_1 v\right]=0. \end{cases} \tag{3.1}$$

For notational convenience, we define $C_1 = \gamma+\beta_2 A+\beta_3\eta$ and $C_2 = \beta_2-\gamma_1$.

3.1. Boundary equilibria

System (1.1) always possesses the trivial equilibrium $E_0(0,0)$. The predator-free equilibrium $E_1(u^*,0)$ with $u^* = K(1-\beta_1\eta/r)$ exists if and only if $r > \beta_1\eta$. The prey-free equilibrium $E_2(0,v^*)$ with $v^* = C_1/(\gamma_1-\beta_2)$ exists if and only if $\gamma_1 > \beta_2$.

3.2. Coexistence equilibria

We focus on the interior equilibria $E_* = (u_*, v_*)$ with $u_* > 0$ and $v_* > 0$. From the first equation of (3.1), one obtains

$$r\left(1-\frac{u_*}{K}\right)-\beta_1\eta = \frac{\alpha v_*}{u_*+mv_*}.$$

For convenience, define

$$R(u) := r\left(1-\frac{u}{K}\right)-\beta_1\eta.$$

Then the relation above can be rewritten as

$$R(u_*)(u_*+mv_*) = \alpha v_*,$$

and hence

$$v_* = \frac{u_*R(u_*)}{\alpha - mR(u_*)}. \tag{3.2}$$

Since $u_* > 0$ and $v_* > 0$, the numerator and denominator in (3.2) must have the same sign. Equivalently, because

$$\frac{\alpha v_*}{u_*+mv_*} > 0 \quad \text{and} \quad \frac{\alpha v_*}{u_*+mv_*} < \frac{\alpha}{m},$$

we require

$$0 < R(u_*) < \frac{\alpha}{m}.$$

The condition $R(u_*) > 0$ gives

$$u_* < K\left(1-\frac{\beta_1\eta}{r}\right) := U,$$

while $R(u_*) < \alpha/m$ gives

$$u_* > K\left(1-\frac{\alpha+m\beta_1\eta}{rm}\right) := L.$$

Therefore, the admissible range for the prey component of a coexistence equilibrium is

$$u_* \in (L_0, U), \qquad L_0 := \max\{0, L\}, \tag{3.3}$$

provided that $U > 0$. Here

$$L = K\left(1-\frac{\alpha+m\beta_1\eta}{rm}\right), \qquad U = K\left(1-\frac{\beta_1\eta}{r}\right).$$

Substituting $v(u_*)$ into the second equation of (3.1) leads to the requirement that u_* must be a root of the following quadratic equation:

$$f(u) := \mathcal{A}u^2 + \mathcal{B}u + C = 0, \quad u \in (L, U). \tag{3.4}$$

The coefficients are given by

$$\begin{aligned} \mathcal{A} &= \beta(rm)^2 + \alpha K r C_2, \\ \mathcal{B} &= 2\beta rm\Theta - \alpha K rm C_1 - \alpha K^2(r - \beta_1\eta)C_2, \\ \mathcal{C} &= \beta\Theta^2 - \alpha K\Theta C_1, \end{aligned} \tag{3.5}$$

where $\Theta = K(\alpha - mr + m\beta_1\eta)$. The existence and multiplicity of equilibria depend on the signs of $f(u)$ at the boundaries

$$f(U) = \alpha^2(\beta - C_1) \quad \text{and} \quad f(L) = -\frac{\alpha^2 K^2 L C_2}{m}. \tag{3.6}$$

Theorem 3.1. *Assume $r > \beta_1\eta$. Let $\Delta = \mathcal{B}^2 - 4\mathcal{A}\mathcal{C}$ be the discriminant of* (3.4) *and $u_{axis} = -\mathcal{B}/(2\mathcal{A})$ be the symmetry axis of the parabola.*

(a) If $f(L)f(U) < 0$, System (1.1) *admits a unique coexistence equilibrium E_*. This occurs if*

- *The Allee effect is weak ($\gamma_1 > \beta_2$) and $\beta < C_1$; or*
- *The Allee effect is strong ($\gamma_1 < \beta_2$) and $\beta > C_1$.*

(b) If $f(L)$ and $f(U)$ have the same sign, up to two equilibria may exist.

- *If $f(L) > 0$ and $f(U) > 0$ (weak Allee, $\beta > C_1$): Two equilibria exist if $\mathcal{A} > 0, \Delta > 0$, and $L < u_{axis} < U$.*
- *If $f(L) < 0$ and $f(U) < 0$ (strong Allee, $\beta < C_1$): Two equilibria exist if $\mathcal{A} < 0, \Delta > 0$, and $L < u_{axis} < U$.*

Proof. For an interior equilibrium $E_* = (u_*, v_*)$, the first equilibrium equation allows us to express v_* as a function of u_*

$$v_* = \frac{u_* R(u_*)}{\alpha - mR(u_*)}, \qquad R(u) = r\left(1 - \frac{u}{K}\right) - \beta_1\eta.$$

The positivity condition $v_* > 0$ requires

$$u_* \in (L_0, U), \qquad L_0 := \max\{0, L\}.$$

Substituting $v_* = v(u_*)$ into the second equilibrium equation reduces the coexistence equilibrium problem to the scalar equation

$$f(u) = \mathcal{A}u^2 + \mathcal{B}u + \mathcal{C} = 0, \qquad u \in (L_0, U).$$

Once an admissible root $u_* \in (L_0, U)$ is obtained, the corresponding $v_* = v(u_*)$ is uniquely determined and positive. Therefore, the number of coexistence equilibria is exactly the number of roots of $f(u) = 0$ in (L_0, U).

We first consider Case (a), where

$$f(L_0)f(U) < 0.$$

By the intermediate value theorem, there is at least one root of f in (L_0, U). We now prove that this root is unique. Suppose, by contradiction, that f has two distinct roots $u_1, u_2 \in (L_0, U)$, with $u_1 < u_2$. If $\mathcal{A} \neq 0$, then

$$f(u) = \mathcal{A}(u - u_1)(u - u_2).$$

Since $L_0 < u_1 < u_2 < U$, we have

$$(L_0 - u_1)(L_0 - u_2) > 0, \qquad (U - u_1)(U - u_2) > 0.$$

Thus, $f(L_0)$ and $f(U)$ must have the same sign, which contradicts $f(L_0)f(U) < 0$. Hence, f cannot have two distinct roots in (L_0, U). If $\mathcal{A} = 0$, then f is linear, and the sign change condition also implies a unique root. Therefore, in Case (a), there is exactly one admissible root u_* and hence exactly one coexistence equilibrium $E_* = (u_*, v_*)$.

For Case (b), $f(L_0)$ and $f(U)$ have the same sign. Since f is a quadratic polynomial, the roots in (L_0, U) can occur only when the vertex lies inside the admissible interval and the extremum crosses the u-axis. This is equivalent to requiring

$$\Delta > 0, \qquad L_0 < u_{\text{axis}} < U, \qquad u_{\text{axis}} = -\frac{\mathcal{B}}{2\mathcal{A}},$$

together with the sign condition stated in the theorem. In this situation, up to two admissible roots (and hence up to two coexistence equilibria) may exist. □

Remark 3.1. Case (b) is of particular ecological interest, as it suggests the potential for a saddle-node bifurcation and bistability, where the population may switch between extinction and survival depending on initial densities.

4. Linear stability and bifurcation analysis

In this section, we investigate the stability of the constant coexistence equilibrium $E_* = (u_*, v_*)$, the existence of Turing patterns induced by prey-taxis, and the occurrence of delay-induced Hopf bifurcations.

4.1. Linearization and characteristic equation

Let $E_* = (u_*, v_*)$ be the spatially homogeneous coexistence equilibrium of System (1.1). We introduce the perturbation variables $\tilde{u}(x, t) = u(x, t) - u_*$ and $\tilde{v}(x, t) = v(x, t) - v_*$. Since E_* is spatially homogeneous, one has $\nabla u_* = 0, \nabla v_* = 0$.

We first clarify the linearization of the memory-based prey-taxis term. Let

$$u(x, t) = u_* + \tilde{u}(x, t), \qquad v(x, t) = v_* + \tilde{v}(x, t),$$

where $\tilde{u}$ and $\tilde{v}$ are small perturbations. Since $E_* = (u_*, v_*)$ is spatially homogeneous, one has

$$\nabla u_* = 0, \qquad \Delta u_* = 0.$$

Hence

$$\nabla u(x, t - \tau) = \nabla \tilde{u}(x, t - \tau), \qquad \Delta u(x, t - \tau) = \Delta \tilde{u}(x, t - \tau).$$

Substituting the perturbation variables into the memory-taxis term gives

$$-\chi \nabla \cdot (v \nabla u(x, t - \tau)) = -\chi \nabla \cdot [(v_* + \tilde{v}(x, t)) \nabla \tilde{u}(x, t - \tau)].$$

Expanding the divergence, we obtain

$$\begin{aligned}-\chi\nabla\cdot\left[(v_*+\tilde{v}(x,t))\nabla\tilde{u}(x,t-\tau)\right] = &-\chi v_*\Delta\tilde{u}(x,t-\tau)\\ &-\chi\nabla\tilde{v}(x,t)\cdot\nabla\tilde{u}(x,t-\tau)\\ &-\chi\tilde{v}(x,t)\Delta\tilde{u}(x,t-\tau).\end{aligned}\tag{4.1}$$

The first term on the right-hand side of (4.1) is linear in the perturbation variables and is retained in the linearized system. The last two terms, namely

$$-\chi\nabla\tilde{v}(x,t)\cdot\nabla\tilde{u}(x,t-\tau)\quad\text{and}\quad-\chi\tilde{v}(x,t)\Delta\tilde{u}(x,t-\tau),$$

are both quadratic terms, because each contains a product of two perturbation quantities. More precisely, if $\tilde{u}$ and $\tilde{v}$ are of order ε, then

$$\nabla\tilde{v}\cdot\nabla\tilde{u}(x,t-\tau)=O(\varepsilon^2),\qquad\tilde{v}\,\Delta\tilde{u}(x,t-\tau)=O(\varepsilon^2).$$

These two terms are therefore neglected in the linearization and included in the higher-order nonlinear remainder. Consequently, the linear contribution of the memory-taxis term is

$$-\chi v_*\Delta\tilde{u}(x,t-\tau).$$

Consequently, the linearized system around E_* is

$$\begin{pmatrix}\tilde{u}_t\\ \tilde{v}_t\end{pmatrix}=D\Delta\begin{pmatrix}\tilde{u}\\ \tilde{v}\end{pmatrix}+B\Delta\begin{pmatrix}\tilde{u}(t-\tau)\\ \tilde{v}(t-\tau)\end{pmatrix}+J\begin{pmatrix}\tilde{u}\\ \tilde{v}\end{pmatrix},\tag{4.2}$$

where

$$D=\begin{pmatrix}d_1&0\\0&d_2\end{pmatrix},\qquad B=\begin{pmatrix}0&0\\-\chi v_*&0\end{pmatrix},\qquad J=\begin{pmatrix}a_{11}&a_{12}\\a_{21}&a_{22}\end{pmatrix}.\tag{4.3}$$

Here, D is the diffusion matrix, B is the delayed taxis matrix, and J is the Jacobian matrix of the reaction terms evaluated at E_*. More precisely, we have

$$\begin{aligned}a_{11}&=r\left(1-\frac{2u_*}{K}\right)-\frac{\alpha m v_*^2}{(u_*+mv_*)^2}-\beta_1\eta,\\ a_{12}&=-\frac{\alpha u_*^2}{(u_*+mv_*)^2}<0,\\ a_{21}&=\frac{\beta m v_*^2}{(u_*+mv_*)^2}+\beta_2 v_*,\\ a_{22}&=\frac{\beta u_*^2}{(u_*+mv_*)^2}-\gamma-\beta_2(A-u_*)-\beta_3\eta-2\gamma_1 v_*.\end{aligned}\tag{4.4}$$

Let μ_k ($k\in\mathbb{N}_0$) be the eigenvalues of $-\Delta$ under homogeneous Neumann boundary conditions, with

$$0=\mu_0<\mu_1\le\mu_2\le\cdots.$$

Expanding $(\tilde{u},\tilde{v})$ in the corresponding Neumann eigenfunctions and restricting (4.2) to the k-th spatial mode, we obtain the characteristic equation

$$\lambda^2+P_k\lambda+Q_k+R_ke^{-\lambda\tau}=0,\qquad k\in\mathbb{N}_0,\tag{4.5}$$

where

$$\begin{aligned} P_k &= (d_1 + d_2)\mu_k - (a_{11} + a_{22}), \\ Q_k &= (d_1\mu_k - a_{11})(d_2\mu_k - a_{22}) - a_{12}a_{21}, \\ R_k &= a_{12}\chi v_*\mu_k. \end{aligned} \tag{4.6}$$

Since $a_{12} < 0, \chi > 0, v_* > 0$, and $\mu_k \geq 0$, one has $R_k \leq 0$, with $R_0 = 0$. Thus, the delayed memory-taxis feedback affects only the nonzero spatial modes.

4.2. Stabilizing effect of prey-taxis for $\tau = 0$

In this subsection, we analyze the case without delay ($\tau = 0$). Unlike the classical approach, where taxis induces instability, here, we investigate the scenario where the system is already unstable under pure diffusion, and we demonstrate how prey-taxis acts as a stabilizing mechanism.

The characteristic equation for the linearized system around E_* is given by

$$\lambda^2 - \mathcal{T}_k\lambda + \mathcal{D}_k(\chi) = 0, \quad k \in \mathbb{N}, \tag{4.7}$$

where the trace $\mathcal{T}_k$ and the determinant $\mathcal{D}_k(\chi)$ are

$$\mathcal{T}_k = (a_{11} + a_{22}) - (d_1 + d_2)\mu_k, \tag{4.8}$$

$$\mathcal{D}_k(\chi) = \underbrace{(d_1\mu_k - a_{11})(d_2\mu_k - a_{22}) - a_{12}a_{21}}_{\mathcal{D}_k^{(0)}} + \chi \underbrace{|a_{12}|v_*\mu_k}_{\mathcal{H}_k}. \tag{4.9}$$

Here, we explicitly use $|a_{12}|$ (since $a_{12} < 0$) to highlight that the contribution of taxis $\mathcal{H}_k = |a_{12}|v_*\mu_k$ is strictly positive for $k > 0$. Consequently, $\mathcal{D}_k(\chi)$ is a strictly increasing function of χ.

We assume the following conditions.

(H_1) The nonspatial ordinary differential equation system is stable ($\mathcal{T}_0 < 0, \mathcal{D}_0 > 0$). This ensures $\mathcal{T}_k < 0$ for all k.

(H_2) The system exhibits Turing instability in the absence of taxis ($\chi = 0$). This implies that there is a set of unstable wavenumbers $\mathbb{K}_u = \{k \in \mathbb{N} \mid \mathcal{D}_k^{(0)} < 0\}$.

Under (H_2), when $\chi = 0$, the system generates spatial patterns corresponding to the modes in $\mathbb{K}_u$. As the prey-taxis sensitivity χ increases, the determinant $\mathcal{D}_k(\chi)$ increases. The equilibrium E_* regains stability when $\mathcal{D}_k(\chi) > 0$ for all $k \in \mathbb{K}_u$.

We define the critical stabilizing taxis value for each unstable mode $k \in \mathbb{K}_u$ as the root of $\mathcal{D}_k(\chi) = 0$

$$\chi_k = \frac{-\mathcal{D}_k^{(0)}}{\mathcal{H}_k} = \frac{-(d_1\mu_k - a_{11})(d_2\mu_k - a_{22}) + a_{12}a_{21}}{|a_{12}|v_*\mu_k} > 0. \tag{4.10}$$

Thus, we define the global critical threshold χ_c as follows:

$$\chi_c = \max_{k \in \mathbb{K}_u} \chi_k. \tag{4.11}$$

Theorem 4.1. *Assume (H_1) and (H_2) hold. For System (1.1) with $\tau = 0$:*

(i) If $0 \leq \chi < \chi_c$, the coexistence equilibrium E_* remains unstable, and spatial patterns (Turing structures) persist.

(ii) If $\chi > \chi_c$, the equilibrium E_* becomes locally asymptotically stable.

(iii) At $\chi = \chi_c$, the system undergoes a bifurcation where the spatial patterns corresponding to the critical mode vanish, marking the transition from a patterned state to a homogeneous state.

This result indicates that attractive prey-taxis serves as a stabilizing force that is capable of suppressing diffusion-driven Turing patterns.

Proof. (i) If $\chi < \chi_c$, by the definition of the maximum, at least one mode $k \in \mathbb{K}_u$ exists such that $\chi < \chi_k$. Since $\mathcal{D}_k(\chi)$ is increasing and $\mathcal{D}_k(\chi_k) = 0$, it implies $\mathcal{D}_k(\chi) < 0$. A negative determinant with a negative trace implies a positive real eigenvalue, maintaining instability.

(ii) If $\chi > \chi_c$, then for all $k \in \mathbb{K}_u$, we have $\chi > \chi_k$, which implies $\mathcal{D}_k(\chi) > 0$. For the modes $k \notin \mathbb{K}_u$ (stable under pure diffusion), $\mathcal{D}_k(\chi) > \mathcal{D}_k^{(0)} > 0$ holds trivially. Thus, $\mathcal{D}_k(\chi) > 0$ for all k. Combined with $\mathcal{T}_k < 0$, all eigenvalues have negative real parts, ensuring the global stability of the linearized system. □

4.3. Delay-induced Hopf bifurcation

In this subsection, we investigate the stability of the coexistence equilibrium E_* as the delay τ increases from zero. We assume that Conditions (H_1) and (H_2) hold, ensuring that E_* is stable when $\tau = 0$. We look for purely imaginary roots $\lambda = i\omega$ ($\omega > 0$) of the characteristic Equation (4.5).

For a fixed spatial mode $k \in \mathbb{N}_0$, substituting $\lambda = i\omega$ into Eq (4.5) yields

$$(i\omega)^2 + P_k(i\omega) + Q_k + R_k e^{-i\omega\tau} = 0. \tag{4.12}$$

Separating the real and imaginary parts, we obtain

$$\begin{cases} \omega^2 - Q_k = R_k \cos(\omega\tau), \\ P_k\omega = R_k \sin(\omega\tau). \end{cases} \tag{4.13}$$

Squaring and adding the two equations in (4.13) eliminates the delay term τ

$$(\omega^2 - Q_k)^2 + (P_k\omega)^2 = R_k^2(\cos^2(\omega\tau) + \sin^2(\omega\tau)) = R_k^2. \tag{4.14}$$

This leads to a fourth-order polynomial equation with respect to ω

$$\omega^4 + (P_k^2 - 2Q_k)\omega^2 + (Q_k^2 - R_k^2) = 0. \tag{4.15}$$

Let $z = \omega^2$. Then Eq (4.15) reduces to a quadratic equation

$$F_k(z) := z^2 + \mathcal{B}_k z + C_k = 0, \tag{4.16}$$

where the coefficients are defined as follows:

$$\mathcal{B}_k = P_k^2 - 2Q_k, \quad C_k = Q_k^2 - R_k^2. \tag{4.17}$$

Since we require $\omega > 0$, we are interested in the positive real roots z of Eq (4.16). According to the distribution of roots for quadratic equations, we have the following lemma regarding the existence of valid oscillation frequencies.

Lemma 4.2. *For a given mode k, Eq* (4.16) *has positive real roots if and only if one of the following conditions is satisfied:*

(i) $C_k < 0$*; in this case, there is a unique positive root* z_k^+.

(ii) $C_k > 0$, $\mathcal{B}_k < 0$, *and* $\Delta_k = \mathcal{B}_k^2 - 4C_k > 0$*; in this case, there are two positive roots* $z_k^\pm$.

We denote the set of indices k for which positive roots exist as $\mathbb{K} = \{k \in \mathbb{N}_0 \mid$ *Eq* (4.16) *admits positive roots*$\}$.

Remark 4.1. The second case in Lemma 4.2 is closely related to the possible stability switch phenomenon. For each fixed spatial mode k, write

$$h_k(z) := z^2 + \mathcal{B}_k z + C_k, \qquad z = \omega^2.$$

If

$$C_k > 0, \qquad \mathcal{B}_k < 0, \qquad \Delta_k = \mathcal{B}_k^2 - 4C_k > 0,$$

then $h_k(z) = 0$ has two positive roots

$$z_k^- = \frac{-\mathcal{B}_k - \sqrt{\Delta_k}}{2}, \qquad z_k^+ = \frac{-\mathcal{B}_k + \sqrt{\Delta_k}}{2}, \qquad 0 < z_k^- < z_k^+.$$

Correspondingly, there are two critical frequencies

$$\omega_k^- = \sqrt{z_k^-}, \qquad \omega_k^+ = \sqrt{z_k^+},$$

and two families of critical delays

$$\{\tau_{k,j}^-\}_{j\geq 0}, \qquad \{\tau_{k,j}^+\}_{j\geq 0}.$$

To determine whether these critical delays lead to stability switches, one has to examine the crossing direction of the characteristic roots. Differentiating the characteristic equation with respect to τ gives the transversality relation

$$\operatorname{sign} \left.\frac{d\,\mathrm{Re}\,\lambda(\tau)}{d\tau}\right|_{\tau=\tau_{k,j}^\pm} = \operatorname{sign} h_k'(z_k^\pm).$$

Since

$$h_k'(z_k^-) = 2z_k^- + \mathcal{B}_k = -\sqrt{\Delta_k} < 0,$$

and

$$h_k'(z_k^+) = 2z_k^+ + \mathcal{B}_k = \sqrt{\Delta_k} > 0,$$

the two Hopf branches generated by z_k^- and z_k^+ have opposite crossing directions. Therefore, when the corresponding critical delay sequences are interlaced, the roots may alternately cross into and out of the right half-plane as τ increases, producing stability switches.

Thus, the two-positive-root case in Lemma 4.2 provides the mechanism for possible delay-induced stability switches. The actual switch points for the full reaction–diffusion system are determined by the ordered set of all critical delays over the admissible modes $k \in \mathbb{K}$.

If $k \in \mathbb{K}$, let $\omega_k = \sqrt{z_k}$ be a positive root. From Eq (4.13), the corresponding critical time delays $\tau_{k,j}$ can be solved. Note that $R_k \leq 0$ (due to prey-taxis; see (4.6)) and $P_k > 0$ (trace condition). From the second equation of (4.13), $\sin(\omega\tau) = P_k\omega/R_k < 0$. Thus, $\omega\tau$ must be in the interval $(2j\pi + \pi, 2j\pi + 2\pi)$. The critical delays are given by

$$\tau_{k,j}^{\pm} = \frac{1}{\omega_k^{\pm}}\left[2(j+1)\pi - \arccos\left(\frac{(\omega_k^{\pm})^2 - Q_k}{R_k}\right)\right], \quad j \in \mathbb{N}_0. \tag{4.18}$$

To verify the Hopf bifurcation conditions, we check the transversality condition. Differentiating the characteristic equation with respect to τ, we obtain

$$\left(\frac{d\lambda}{d\tau}\right)^{-1} = \frac{2\lambda + P_k}{-\lambda(\lambda^2 + P_k\lambda + Q_k)} - \frac{\tau}{\lambda}. \tag{4.19}$$

Evaluating the real part at $\lambda = i\omega_k$, following the method in Song et al., we have

$$\operatorname{sgn}\left\{\operatorname{Re}\left(\frac{d\lambda}{d\tau}\right)\Big|_{\tau=\tau_{k,j}^{\pm}}\right\} = \operatorname{sgn}\{F_k'(z_k^{\pm})\} = \operatorname{sgn}\{2z_k^{\pm} + \mathcal{B}_k\} = \operatorname{sgn}\left\{\pm\sqrt{\Delta_k}\right\}. \tag{4.20}$$

Therefore, we have the following.

(i) For the root z_k^+ (derived from $+\sqrt{\Delta_k}$), the transversality sign is positive, implying a cross from left to right (destabilizing).
(ii) For the root z_k^- (derived from $-\sqrt{\Delta_k}$), the transversality sign is negative, implying a cross from right to left (stabilizing).

Define the minimal critical delay as

$$\tau_* = \min\{\tau_{k,0}^+ \mid k \in \mathbb{K}\}. \tag{4.21}$$

On the basis of the analysis above, we establish the following theorem on delay-induced instability.

Theorem 4.3. *Assume that Conditions* (H_1) *and* (H_2) *hold.*

(i) If $\mathbb{K} = \emptyset$*, i.e., for all* $k \in \mathbb{N}_0$*,* $C_k \geq 0$ *and* $\mathcal{B}_k \geq 0$*, then System* (1.1) *admits no stability switches. The coexistence equilibrium* E_* *remains locally asymptotically stable for all* $\tau \geq 0$*.*

(ii) If $\mathbb{K} \neq \emptyset$*, then* E_* *is locally asymptotically stable for* $\tau \in [0, \tau_*)$*.*

(iii) At $\tau = \tau_*$*, corresponding to a critical mode* $k_* \in \mathbb{K}$*, the system undergoes a Hopf bifurcation.*

(a) If $k_* = 0$*, the bifurcation leads to spatially homogeneous periodic solutions.*
(b) If $k_* > 0$*, the bifurcation leads to spatially nonhomogeneous periodic solutions.*

5. Normal form of Hopf bifurcation

This section derives the normal form of the Hopf bifurcation at the critical delay $\tau = \tau_c$. The calculation follows the center manifold reduction for the partial functional differential equations developed in [36]. Although the well-posedness and linear stability results in the previous sections are formulated

for general bounded domains $\Omega \subset \mathbb{R}^n$, $n = 1, 2, 3$, the explicit normal form calculation is carried out on the one-dimensional interval $\Omega = (0, l\pi)$ with homogeneous Neumann boundary conditions. This restriction is made for analytical tractability, since the computation of the normal form coefficients requires the products and integrals of Neumann eigenfunctions. On $(0, l\pi)$, these eigenfunctions have the explicit form

$$\beta_k(x) = \cos\frac{kx}{l}, \qquad k = 0, 1, 2, \ldots,$$

which allows the projection formulas and the cubic normal form coefficient to be evaluated explicitly.

Let $E_* = (u_*, v_*)$ be a positive constant equilibrium of System (1.1). Set

$$U(x,t) = u(x,t) - u_*, \qquad V(x,t) = v(x,t) - v_*, \qquad \mathbf{U}(t) = (U(\cdot,t), V(\cdot,t))^{\mathrm{T}}.$$

For the Neumann Laplacian on $(0, l\pi)$, write

$$\mu_n = \frac{n^2}{l^2}, \qquad \beta_n(x) = \cos\frac{nx}{l}, \qquad n = 0, 1, 2, \ldots.$$

In what follows, $n \geq 1$ denotes the critical spatial mode associated with the Hopf bifurcation.

Let

$$S_* := u_* + mv_*.$$

The Jacobian matrix of the reaction terms at E_* is denoted by

$$J = \begin{pmatrix} a_{11} & a_{12} \\ a_{21} & a_{22} \end{pmatrix},$$

where

$$a_{11} = r\left(1 - \frac{2u_*}{K}\right) - \frac{\alpha m v_*^2}{S_*^2} - \beta_1\eta, \qquad a_{12} = -\frac{\alpha u_*^2}{S_*^2}, \tag{5.1}$$

$$a_{21} = \frac{\beta m v_*^2}{S_*^2} + \beta_2 v_*, \qquad a_{22} = \frac{\beta u_*^2}{S_*^2} - \gamma - \beta_2(A - u_*) - \beta_3\eta - 2\gamma_1 v_*. \tag{5.2}$$

The diffusion and memory-taxis matrices are

$$D = \begin{pmatrix} d_1 & 0 \\ 0 & d_2 \end{pmatrix}, \qquad B = \begin{pmatrix} 0 & 0 \\ -\chi v_* & 0 \end{pmatrix}.$$

Introduce the rescaled time so that the delay interval becomes $[-1, 0]$, and write $\tau = \tau_c + \mu$, where μ is the bifurcation parameter. Let

$$C = C([-1, 0]; X), \qquad X = (L^2(0, l\pi))^2.$$

For $\phi \in C$, write

$$\phi(\theta) = (\phi_1(\theta), \phi_2(\theta))^{\mathrm{T}}, \qquad -1 \leq \theta \leq 0.$$

Then the perturbed system can be written as the abstract partial functional differential equation (PFDE)

$$\dot{\mathbf{U}}(t) = L_\mu(\mathbf{U}_t) + F(\mathbf{U}_t, \mu), \tag{5.3}$$

where

$$\mathbf{U}_t(\theta) = \mathbf{U}(t+\theta), \qquad -1 \le \theta \le 0,$$

and

$$L_\mu(\phi) = (\tau_c + \mu)\left[D\Delta\phi(0) + B\Delta\phi(-1) + J\phi(0)\right]. \tag{5.4}$$

The infinitesimal generator associated with L_0 is denoted by $\mathcal{A}$. It is given by

$$\mathcal{A}\phi = \dot{\phi},$$

with the domain

$$\mathcal{D}(\mathcal{A}) = \left\{\phi \in C : \dot{\phi} \in C,\ \phi(0) \in \mathcal{D}(\Delta),\ \dot{\phi}(0) = L_0(\phi)\right\}.$$

For the n-th spatial mode, the characteristic equation is

$$\lambda^2 + P_n\lambda + Q_n + R_n e^{-\lambda\tau} = 0, \tag{5.5}$$

where

$$P_n = (d_1 + d_2)\mu_n - (a_{11} + a_{22}), \tag{5.6}$$
$$Q_n = (d_1\mu_n - a_{11})(d_2\mu_n - a_{22}) - a_{12}a_{21}, \tag{5.7}$$
$$R_n = a_{12}\chi v_*\mu_n. \tag{5.8}$$

Assume that for $\tau = \tau_c$, Equation (5.5) has a simple pair of purely imaginary roots

$$\lambda = \pm i\omega_n, \qquad \omega_n > 0,$$

and that no other root lies on the imaginary axis. Under the time rescaling, $\pm i\omega_n\tau_c$ are the corresponding eigenvalues of $\mathcal{A}$.

The eigenfunction of $\mathcal{A}$ corresponding to $i\omega_n\tau_c$ is

$$q(\theta, x) = p_n e^{i\omega_n\tau_c\theta}\beta_n(x), \qquad -1 \le \theta \le 0, \tag{5.9}$$

where

$$p_n = (1, \xi_n)^{\mathrm{T}}, \qquad \xi_n = \frac{i\omega_n + d_1\mu_n - a_{11}}{a_{12}}.$$

The adjoint eigenfunction corresponding to $-i\omega_n\tau_c$ is written as

$$q^*(s, x) = \mathscr{D}_n p_n^* e^{i\omega_n\tau_c s}\beta_n(x), \qquad 0 \le s \le 1, \tag{5.10}$$

where

$$p_n^* = (1, \rho_n)^{\mathrm{T}}, \qquad \rho_n = \frac{a_{12}}{-i\omega_n + d_2\mu_n - a_{22}}.$$

The constant $\mathscr{D}_n$ is chosen so that

$$\langle q^*, q\rangle = 1.$$

Here, $\langle\cdot,\cdot\rangle$ denotes the standard bilinear form for PFDEs. For the n-th spatial mode, it is induced by the linear operator

$$\tau_c\left[(J - \mu_n D)\phi(0) - \mu_n B\phi(-1)\right].$$

Next, the nonlinear part is expanded at E_*. Define

$$H(U,V)=\frac{(u_*+U)(v_*+V)}{u_*+U+m(v_*+V)}.$$

Then

$$H(0,0)=\frac{u_*v_*}{S_*},\qquad H_U(0,0)=\frac{mv_*^2}{S_*^2},\qquad H_V(0,0)=\frac{u_*^2}{S_*^2}.$$

For $\phi\in C$, the nonlinear term in (5.3) is

$$F(\phi,\mu)=(\tau_c+\mu)\begin{pmatrix}N_1(\phi)\\N_2(\phi)\end{pmatrix},\tag{5.11}$$

where

$$N_1(\phi)=-\frac{r}{K}\phi_1^2(0)-\alpha\Big[H(\phi_1(0),\phi_2(0))-H(0,0)-H_U(0,0)\phi_1(0)-H_V(0,0)\phi_2(0)\Big],\tag{5.12}$$

$$\begin{aligned}N_2(\phi)=&-\chi\nabla\cdot(\phi_2(0)\nabla\phi_1(-1))+\beta\Big[H(\phi_1(0),\phi_2(0))-H(0,0)-H_U(0,0)\phi_1(0)-H_V(0,0)\phi_2(0)\Big]\\&+\beta_2\phi_1(0)\phi_2(0)-\gamma_1\phi_2^2(0).\end{aligned}\tag{5.13}$$

Thus the expansion of $F(\phi,0)$ has the form

$$F(\phi,0)=\frac{1}{2}F_2(\phi,\phi)+\frac{1}{6}F_3(\phi,\phi,\phi)+O(\|\phi\|_C^4),\tag{5.14}$$

where F_2 and F_3 are symmetric multilinear mappings.

For $\phi,\psi\in C$, we have

$$F_2(\phi,\psi)=\tau_c\begin{pmatrix}\mathcal{A}_{20}\phi_1(0)\psi_1(0)+\mathcal{A}_{11}[\phi_1(0)\psi_2(0)+\phi_2(0)\psi_1(0)]+\mathcal{A}_{02}\phi_2(0)\psi_2(0)\\-\chi\left[\nabla\cdot(\phi_2(0)\nabla\psi_1(-1))+\nabla\cdot(\psi_2(0)\nabla\phi_1(-1))\right]\\+\mathcal{B}_{20}\phi_1(0)\psi_1(0)+\mathcal{B}_{11}[\phi_1(0)\psi_2(0)+\phi_2(0)\psi_1(0)]+\mathcal{B}_{02}\phi_2(0)\psi_2(0)\end{pmatrix}.\tag{5.15}$$

For $\phi,\psi,\zeta\in C$, we have

$$F_3(\phi,\psi,\zeta)=\tau_c\begin{pmatrix}\mathfrak{F}_3^{(1)}(\phi,\psi,\zeta)\\\mathfrak{F}_3^{(2)}(\phi,\psi,\zeta)\end{pmatrix},\tag{5.16}$$

where

$$\begin{aligned}\mathfrak{F}_3^{(1)}(\phi,\psi,\zeta)=&\mathcal{A}_{30}\phi_1(0)\psi_1(0)\zeta_1(0)+\mathcal{A}_{21}\sum_{\text{sym}}\phi_1(0)\psi_1(0)\zeta_2(0)\\&+\mathcal{A}_{12}\sum_{\text{sym}}\phi_1(0)\psi_2(0)\zeta_2(0)+\mathcal{A}_{03}\phi_2(0)\psi_2(0)\zeta_2(0),\end{aligned}\tag{5.17}$$

$$\begin{aligned}\mathfrak{F}_3^{(2)}(\phi,\psi,\zeta)=&\mathcal{B}_{30}\phi_1(0)\psi_1(0)\zeta_1(0)+\mathcal{B}_{21}\sum_{\text{sym}}\phi_1(0)\psi_1(0)\zeta_2(0)\\&+\mathcal{B}_{12}\sum_{\text{sym}}\phi_1(0)\psi_2(0)\zeta_2(0)+\mathcal{B}_{03}\phi_2(0)\psi_2(0)\zeta_2(0).\end{aligned}\tag{5.18}$$

In (5.17)–(5.18), $\sum_{\text{sym}}$ denotes the sum over all distinct symmetric permutations of the displayed product.

The coefficients in the quadratic terms are

$$\mathcal{A}_{20} = -\frac{2r}{K} + \frac{2\alpha m v_*^2}{S_*^3}, \qquad \mathcal{A}_{11} = -\frac{2\alpha m u_* v_*}{S_*^3}, \qquad \mathcal{A}_{02} = \frac{2\alpha m u_*^2}{S_*^3}, \tag{5.19}$$

$$\mathcal{B}_{20} = -\frac{2\beta m v_*^2}{S_*^3}, \qquad \mathcal{B}_{11} = \frac{2\beta m u_* v_*}{S_*^3} + \beta_2, \qquad \mathcal{B}_{02} = -\frac{2\beta m u_*^2}{S_*^3} - 2\gamma_1. \tag{5.20}$$

The coefficients in the cubic terms are

$$\mathcal{A}_{30} = -\frac{6\alpha m v_*^2}{S_*^4}, \qquad \mathcal{A}_{21} = \frac{2\alpha m v_*(2u_* - m v_*)}{S_*^4}, \tag{5.21}$$

$$\mathcal{A}_{12} = \frac{2\alpha m u_*(2m v_* - u_*)}{S_*^4}, \qquad \mathcal{A}_{03} = -\frac{6\alpha m^2 u_*^2}{S_*^4}, \tag{5.22}$$

$$\mathcal{B}_{30} = \frac{6\beta m v_*^2}{S_*^4}, \qquad \mathcal{B}_{21} = \frac{2\beta m v_*(m v_* - 2u_*)}{S_*^4}, \tag{5.23}$$

$$\mathcal{B}_{12} = \frac{2\beta m u_*(u_* - 2m v_*)}{S_*^4}, \qquad \mathcal{B}_{03} = \frac{6\beta m^2 u_*^2}{S_*^4}. \tag{5.24}$$

Let

$$\mathcal{P} = \text{span}\{q, \bar{q}\}$$

be the center eigenspace and let Q be its complement. On the center manifold, the solution can be represented as

$$\mathbf{U}_t = zq + \bar{z}\,\bar{q} + W(z, \bar{z}, \theta), \tag{5.25}$$

where

$$z(t) = \langle q^*, \mathbf{U}_t \rangle,$$

and

$$W(z, \bar{z}, \theta) = \frac{1}{2} w_{20}(\theta) z^2 + w_{11}(\theta) z\bar{z} + \frac{1}{2} w_{02}(\theta) \bar{z}^2 + O(|z|^3). \tag{5.26}$$

The reduced equation on the center manifold is

$$\dot{z} = i\omega_n \tau_c z + g(z, \bar{z}), \tag{5.27}$$

where

$$g(z, \bar{z}) = \frac{1}{2} g_{20} z^2 + g_{11} z\bar{z} + \frac{1}{2} g_{02} \bar{z}^2 + \frac{1}{2} g_{21} z^2 \bar{z} + O(|z|^4). \tag{5.28}$$

For $n \geq 1$, the following orthogonality relations hold

$$\int_0^{l\pi} \beta_n^3(x)\, dx = 0, \qquad \int_0^{l\pi} \beta_n(x) |\nabla \beta_n(x)|^2\, dx = 0.$$

Consequently, the quadratic projections onto the critical eigenspace vanish

$$g_{20} = g_{11} = g_{02} = 0. \tag{5.29}$$

It remains to compute g_{21}. The functions w_{20} and w_{11} satisfy the homological equations

$$(2i\omega_n\tau_c I - \mathcal{A})\, w_{20} = F_2(q, q), \tag{5.30}$$

$$-\mathcal{A} w_{11} = F_2(q, \bar{q}). \tag{5.31}$$

Since $2i\omega_n\tau_c$ and 0 are not eigenvalues of $\mathcal{A}$ on $\mathcal{Q}$, these equations determine w_{20} and w_{11} uniquely in the complementary space.

The coefficient g_{21} is then given by

$$g_{21} = \langle q^*, F_3(q, q, \bar{q}) + 2F_2(q, w_{11}) + F_2(\bar{q}, w_{20}) \rangle . \tag{5.32}$$

Equations (5.15), (5.16), (5.30), (5.31), and (5.32) provide a complete calculation of the cubic coefficient in the normal form.

For practical computation, w_{20} and w_{11} may be expanded in the Neumann eigenbasis. Since

$$\beta_n^2(x) = \frac{1}{2}\left(1 + \cos\frac{2nx}{l}\right),$$

one writes

$$w_{20}(\theta, x) = E_{20}^{(0)} e^{2i\omega_n\tau_c\theta} + E_{20}^{(2n)} e^{2i\omega_n\tau_c\theta} \cos\frac{2nx}{l}, \tag{5.33}$$

$$w_{11}(\theta, x) = E_{11}^{(0)} + E_{11}^{(2n)} \cos\frac{2nx}{l}. \tag{5.34}$$

The constant vectors $E_{20}^{(0)}, E_{20}^{(2n)}, E_{11}^{(0)}$, and $E_{11}^{(2n)} \in \mathbb{C}^2$ are obtained by solving the corresponding two-dimensional linear algebraic systems generated by (5.30)–(5.31). This modal representation is often the most convenient form for numerical evaluation of g_{21}.

The first Lyapunov coefficient is defined by

$$c_1(0) = \frac{1}{2} g_{21}. \tag{5.35}$$

The derivative of the critical eigenvalue with respect to the delay is obtained by differentiating (5.5). At $\lambda = i\omega_n$ and $\tau = \tau_c$, we have

$$\lambda'(\tau_c) = \left.\frac{\lambda R_n e^{-\lambda\tau_c}}{2\lambda + P_n - \tau_c R_n e^{-\lambda\tau_c}}\right|_{\lambda = i\omega_n}. \tag{5.36}$$

The transversality condition is

$$\operatorname{Re}\lambda'(\tau_c) \neq 0. \tag{5.37}$$

Define

$$\mu_2^H = -\frac{\operatorname{Re} c_1(0)}{\operatorname{Re}\lambda'(\tau_c)}, \qquad \beta_2^H = 2\operatorname{Re} c_1(0). \tag{5.38}$$

The superscript H is used to distinguish these Hopf normal-form quantities from the model parameter β_2.

Theorem 5.1. *Assume that the characteristic equation* (5.5) *has a simple pair of purely imaginary roots* $\pm i\omega_n$ *at* $\tau = \tau_c$*, and that the transversality condition* (5.37) *holds. Then the Hopf bifurcation of system* (1.1) *at* $\tau = \tau_c$ *has the following properties.*

(i) If $\mu_2^H > 0$ (*respectively* $\mu_2^H < 0$)*, then the Hopf bifurcation is supercritical* (*respectively subcritical*) *and the bifurcating periodic solutions exist for* $\tau > \tau_c$ (*respectively* $\tau < \tau_c$)*.*

(ii) If $\beta_2^H < 0$ (*respectively* $\beta_2^H > 0$)*, then the bifurcating periodic solutions are orbitally asymptotically stable* (*resp. unstable*)*.*

6. Numerical simulations

In this section, we conduct extensive numerical simulations to validate the theoretical findings derived in the previous sections and to explore the complex spatiotemporal dynamics induced by the interplay between memory-based prey-taxis and time delay. The numerical integration is performed using a semi-implicit Euler method for time stepping and a central difference scheme for spatial discretization on a one-dimensional domain $\Omega = [0, L]$. Unless otherwise stated, we fix the spatial length $L = 20$, the grid size $N_x = 200$ (step size $\Delta x = 0.1$), and the time step $\Delta t = 0.005$. The initial conditions are chosen as the coexistence equilibrium E_* with small random spatial perturbations of magnitude 10^{-2}.

The fixed parameters are chosen to satisfy condition (H_2), ensuring that the system exhibits diffusion-driven instability in the absence of taxis and delay. Specifically, we set

$$\begin{aligned} &r = 1.2, \quad K = 2, \quad \alpha = 0.9, \quad m = 0.45, \quad \beta_1 = 0.1, \quad \eta = 1, \\ &\beta = 0.8, \quad \gamma = 0.3, \quad \beta_2 = 0.1, \quad A = 0.1, \quad \beta_3 = 0.1, \quad \gamma_1 = 0.15. \end{aligned} \tag{6.1}$$

The diffusion coefficients are set to $d_1 = 0.01$, and $d_2 = 2.0$, so that the predator has a much larger effective mobility than the prey/resource population. The ratio $d_2 : d_1 = 200 : 1$ is admittedly large, but it should be understood in terms of nondimensional effective diffusion coefficients rather than direct physical diffusion constants. Ecologically, this parameter choice corresponds to a high-mobility predator actively searching over a relatively large spatial range, while the prey/resource population disperses much more slowly and is mainly regulated by local growth and predation. Such a contrast is particularly relevant when the prey is weakly mobile, spatially restricted, or represents a slowly spreading resource, whereas the predator responds actively to prey gradients.

The purpose of this choice is to examine a regime in which the mobility contrast and prey-taxis are strong enough to interact with the local reaction kinetics and generate visible spatial effects. Thus, the ratio $d_2 : d_1 = 200 : 1$ is not intended as a universal empirical value for all predator–prey systems but as a representative high-mobility contrast used to illustrate the mechanism under consideration. Under these parameters, the coexistence equilibrium is calculated as $E_* \approx (0.4643, 0.7191)$.

6.1. Stability map and bifurcation analysis

To provide a global perspective on the system's dynamics, we construct a two-parameter bifurcation diagram in the (χ, τ)-plane, as shown in Figure 1. This stability map delineates the critical boundaries

where the stability of the homogeneous equilibrium E_* transitions, thereby partitioning the parameter space into four distinct dynamic regions. Specifically, the Turing bifurcation boundary, represented by the vertical dashed line at $\chi_c \approx 1.5215$, separates the diffusion-unstable regime ($\chi < \chi_c$) from the diffusion-stable regime ($\chi > \chi_c$). Complementing this, the Hopf bifurcation boundary is illustrated by the solid curve $\tau_*(\chi)$, which is determined as the lower envelope of the stability thresholds across all relevant spatial modes.

As illustrated in Figure 1, the intersection of these boundaries defines four regions: Region I (stable), Region II (Turing pattern), Region III (Hopf bifurcation), and Region IV (interaction). A notable feature is that the critical delay τ_* decreases as χ increases, indicating that strong prey-taxis, while stabilizing spatial patterns, can lower the threshold for temporal oscillations.

To verify these dynamical behaviors, we select four representative points (P_1, P_2, P_3, P_4) as listed in Table 2.

Table 2. Representative parameter sets selected for numerical simulations.

Point	Region	Parameters (χ, τ)	Dynamical Feature
P_1	I (stable)	$(2.0, 3.0)$	Homogeneous steady state
P_2	II (Turing)	$(1.0, 6.0)$	Stationary spatial patterns
P_3	III (Hopf)	$(2.0, 6.0)$	Spatially nonhomogeneous periodic solutions
P_4	IV (interaction)	$(1.4, 7.9)$	Complex spatiotemporal dynamics

6.2. *Spatiotemporal dynamics in different regions*

We now present the spatiotemporal evolution of the prey and predator densities corresponding to the four points selected in Figure 1.

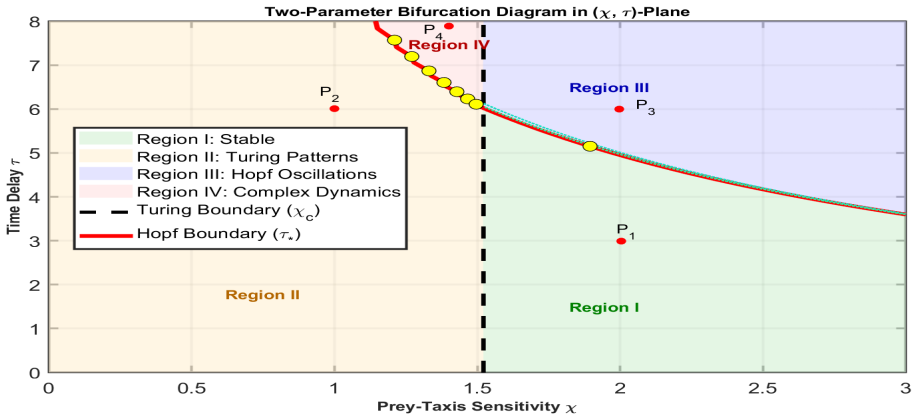

Figure 1. Two-parameter bifurcation diagram in the (χ, τ)-plane. The vertical dashed line represents the Turing threshold $\chi_c \approx 1.5215$, above which diffusion-driven spatial instability is suppressed. The solid red curve represents the Hopf threshold $\tau_*(\chi)$. Its decreasing trend indicates that stronger delayed prey-taxis may lower the critical delay for temporal oscillations. The markers P_1–P_4 indicate the parameter sets used in the simulations.

(i) Stabilization by Prey-Taxis (Region I). Point P_1 with $(\chi, \tau) = (2.0, 3.0)$ is located in Region I. Although the diffusion coefficients satisfy the Turing condition ($d_2 \gg d_1$), the prey-taxis coefficient

$\chi = 2.0$ exceeds the critical threshold χ_c. Furthermore, the time delay $\tau = 3.0$ is below the Hopf threshold $\tau_*(\chi)$. As shown in Figure 2, the initial random perturbations decay rapidly, and the system converges to the spatially homogeneous steady state E_*. This confirms our theoretical result that strong attractive prey-taxis can act as a stabilizing force, suppressing diffusion-driven instability.

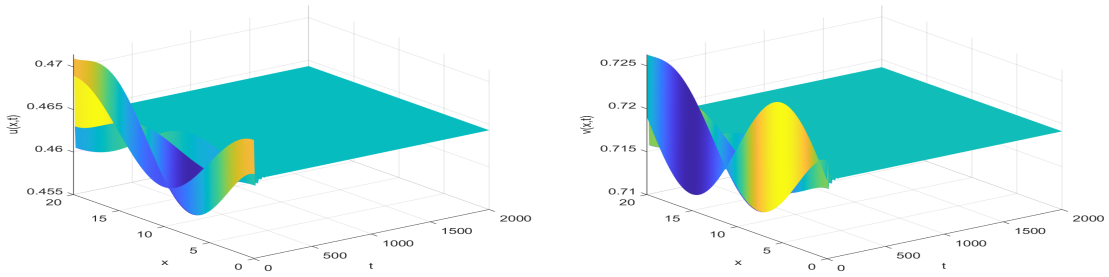

Figure 2. Time evolution at P_1 (Region I). The system converges to the stable homogeneous state E_*.

(ii) Stationary Turing Patterns (Region II). Point P_2 with $(\chi, \tau) = (1.0, 6.0)$ lies in Region II. Here, the taxis coefficient $\chi = 1.0$ is insufficient to stabilize the system ($\chi < \chi_c$). Since the delay is relatively large but the parameters are such that the spatial instability dominates (or the delay does not yet induce oscillations for the dominant modes in this regime), the system evolves into a stationary spatial structure. Figure 3 displays the formation of stable, time-independent spatial stripes (Turing patterns). This demonstrates the classic diffusion-driven instability mechanism.

(iii) Delay-Induced Oscillations (Region III). Point P_3 with $(\chi, \tau) = (2.0, 6.0)$ is located in Region III. Compared with P_1, the taxis coefficient remains high ($\chi = 2.0$), which is sufficient to suppress diffusion-driven patterns. However, the time delay $\tau = 6.0$ significantly exceeds the critical Hopf bifurcation threshold (calculated as $\tau_* \approx 1.23$ for the critical mode $n = 3$). Consequently, the homogeneous equilibrium loses stability. To characterize the nature of this instability, we computed the normal form coefficients at the critical point, yielding $\mu_2 \approx 33.60 > 0$ and $\beta_2 \approx -0.623 < 0$. According to the Hopf bifurcation theorem, $\mu_2 > 0$ indicates a supercritical bifurcation (oscillations emerge for $\tau > \tau_*$) and $\beta_2 < 0$ guarantees that these periodic solutions are orbitally asymptotically stable. This theoretical prediction is fully corroborated by the numerical simulation in Figure 4, where the system exhibits sustained, stable periodic oscillations. Since the instability arises from a nonzero wavenumber ($k \neq 0$), these oscillations manifest as spatially nonhomogeneous patterns, such as standing waves or breathing patterns.

(iv) Complex Spatiotemporal Dynamics (Region IV). Point P_4 with $(\chi, \tau) = (1.4, 7.9)$ falls into Region IV, the interaction region. Here, $\chi < \chi_c$ favors spatial Turing patterns, while $\tau > \tau_*$ favors temporal oscillations. The competition between these two instability mechanisms leads to highly complex dynamics. Figure 5 illustrates irregular spatiotemporal behaviors, where the pattern structure evolves chaotically over time. This suggests the presence of spatiotemporal chaos or mixed-mode oscillations resulting from the Turing–Hopf interaction.

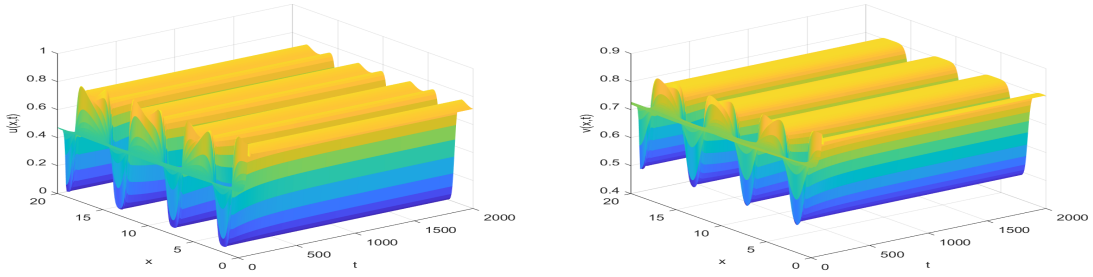

Figure 3. Time evolution at P_2 (Region II). The system forms stationary Turing patterns.

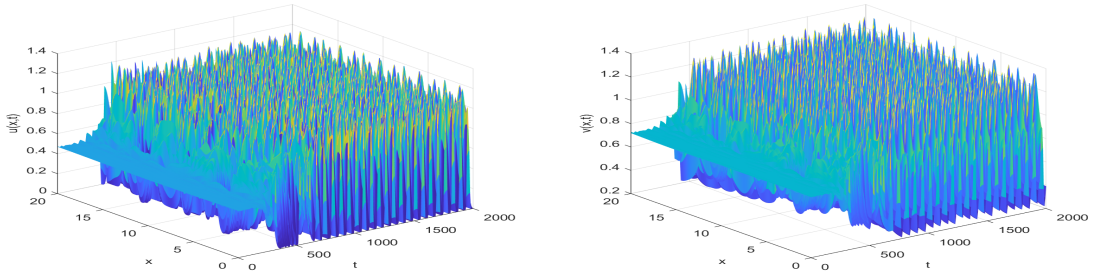

Figure 4. Time evolution at P_3 (Region III). The system exhibits spatially nonhomogeneous periodic oscillations (Hopf).

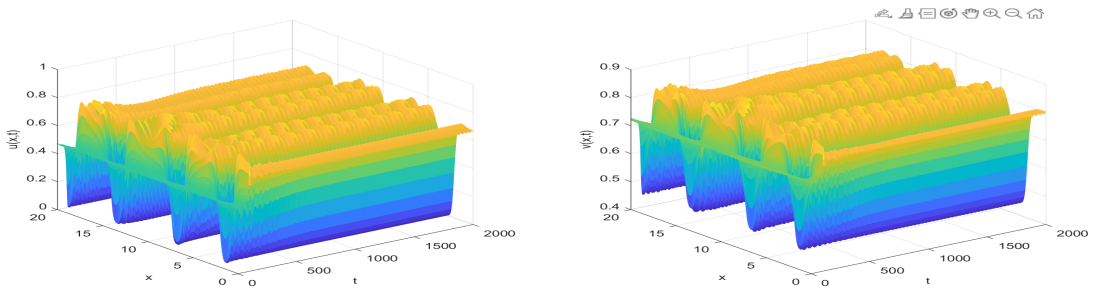

Figure 5. Time evolution at P_4 (Region IV). The system displays complex spatiotemporal dynamics due to Turing–Hopf interaction.

To distinguish Region III from Region IV more clearly, we further examine the temporal signals at several fixed spatial locations and their corresponding power spectra. In Figure 6, we select three representative spatial points $x = L/4$, $x = L/2$, and $x = 3L/4$ and plot the time series of $u(x, t)$ and $v(x, t)$ after removing the initial transient, together with their normalized temporal power spectra.

Figure 6(a)–(b) corresponds to the representative point P_3 in Region III. The time series at the fixed spatial points remain oscillatory and relatively regular, and the corresponding power spectra are highly concentrated around a dominant frequency, with only a few weak secondary components. In particular, the mean spectral entropy is relatively low (0.5535 for u and 0.5999 for v), indicating that the temporal dynamics are mainly governed by a single oscillatory mode. This confirms that Region III is characterized by spatially nonhomogeneous but essentially periodic oscillations.

By contrast, panels Figure 6(c)–(d) corresponds to the representative point P_4 in Region IV. In this case, the time series show stronger amplitude variation and a less regular oscillatory pattern. Moreover,

the corresponding power spectra are distributed over a broader frequency range, and the mean spectral entropy becomes noticeably larger (0.6756 for u and 0.7013 for v). These features indicate that the temporal behavior in Region IV cannot be described by a single dominant periodic mode. Instead, it reflects a more complicated spatiotemporal regime arising from the interaction between delay-induced Hopf oscillations and diffusion-driven spatial instability.

Therefore, Figure 6 provides quantitative evidence for the distinction between the two regimes: Region III corresponds to spatially nonhomogeneous periodic solutions, whereas Region IV exhibits more complex spatiotemporal dynamics.

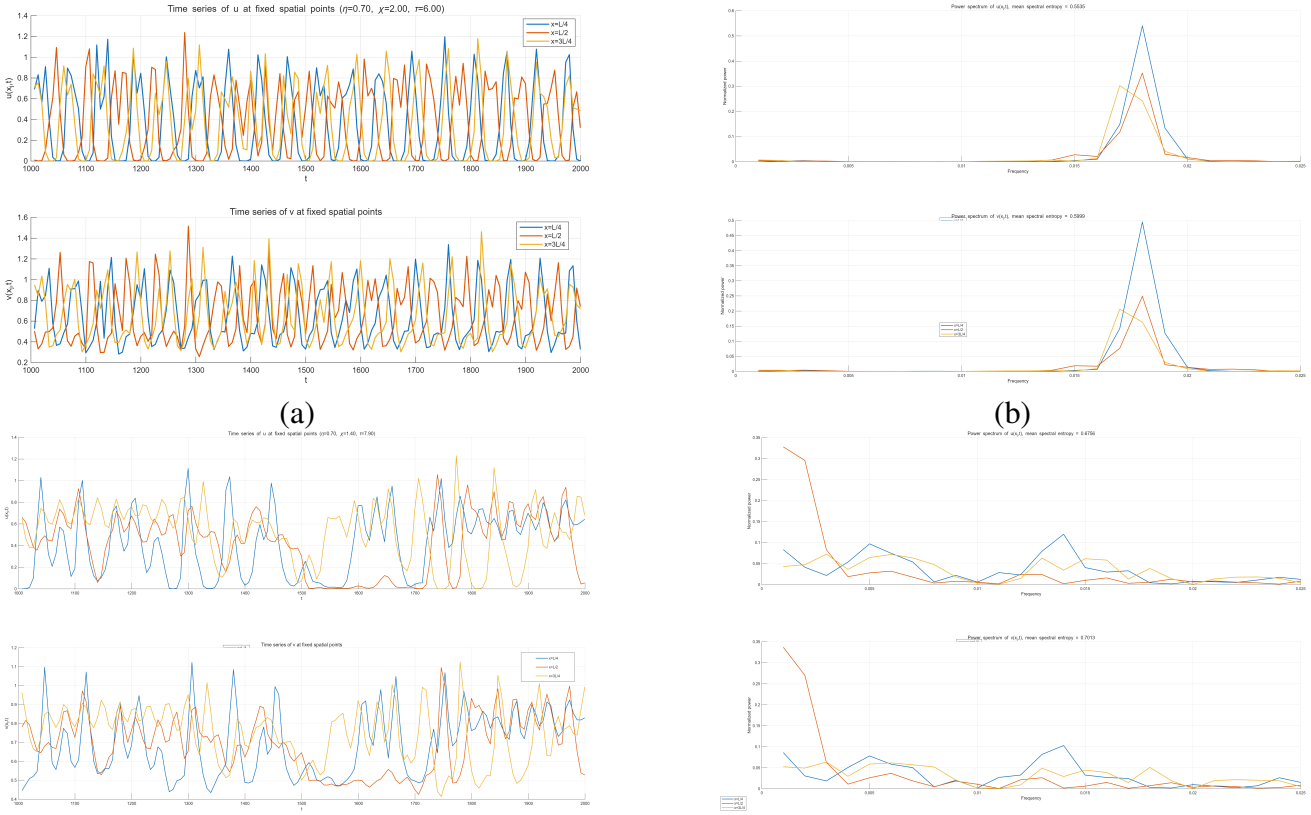

Figure 6. Quantitative comparison between Region III and Region IV. (a) P_3: Time series at fixed spatial points; (b) P_3: Normalized power spectra; (c) P_4: Time series at fixed spatial points; (d) P_4: Normalized power spectra. For P_3, the oscillations are relatively regular and the spectra are concentrated around a dominant frequency, indicating spatially nonhomogeneous periodic behavior. For P_4, the time series show stronger irregularity and the spectra are broader, indicating more complex spatiotemporal dynamics.

6.3. Effect of environmental stress on stability transition

Finally, we investigate the impact of the environmental stressor η on the dynamics of the system. We fix the prey-taxis coefficient at $\chi = 2.0$ and vary η. To distinguish reaction-driven instability from diffusion-driven instability, we combine numerical simulations with the linear stability analysis of the

coexistence equilibrium E_*. In the numerical simulations, the maximum and minimum densities of both prey and predator are recorded after the transient dynamics have decayed.

As shown in Figure 7, the system undergoes three different dynamic regimes as η increases.

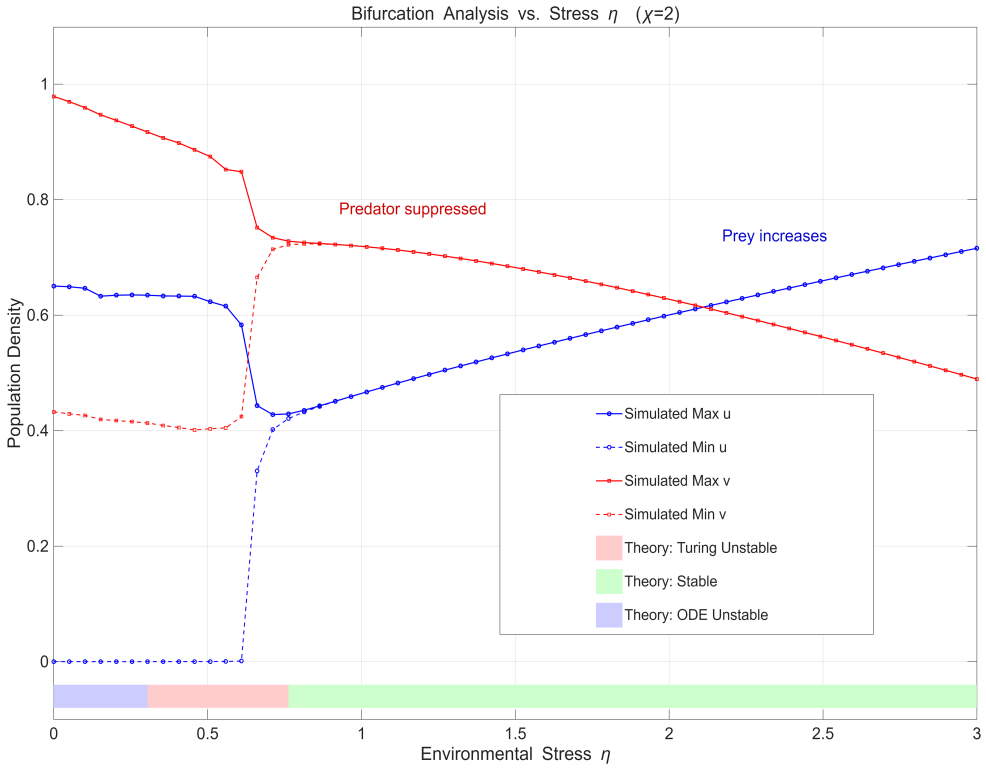

Figure 7. Effect of environmental stress η on the simulated prey and predator densities at $\chi = 2.0$. The blue curves denote the maximum and minimum prey densities, while the red curves denote the maximum and minimum predator densities. The bottom color bar indicates the theoretically predicted stability regimes: ordinary differential equation instability, Turing instability, and stable homogeneous coexistence. In the stable homogeneous regime, the prey density increases, whereas the predator density decreases as η increases, providing direct evidence for the predator release effect.

- **Phase I: ODE instability.** For small environmental stresses, i.e., approximately $\eta \lesssim 0.3$, the linear stability analysis predicts the instability of the spatially homogeneous ODE subsystem. In this regime, the numerical solution displays large spatial variation. The minimum prey density approaches zero, while the maximum prey density remains positive, indicating the emergence of strong patchiness. The predator density also exhibits a clear separation between its maximum and minimum values, reflecting unstable local predator–prey oscillations.
- **Phase II: Turing instability.** For intermediate stress levels, approximately $0.3 \lesssim \eta \lesssim 0.75$, the homogeneous ODE equilibrium becomes locally stable, but the reaction–diffusion system is destabilized by spatial modes. This corresponds to the Turing-unstable region. Numerically, the prey density still exhibits strong spatial heterogeneity, with $u_{\max}$ and $u_{\min}$ remaining clearly separated. The predator density also remains spatially nonuniform, which confirms that the instability is not purely temporal but is associated with spatial pattern formation.

- **Phase III: Stabilization and homogenization.** When η exceeds the critical value $\eta_c \approx 0.75$, the system enters a stable homogeneous coexistence regime. In this region, the maximum and minimum density curves collapse onto single branches for both species, showing that the spatial heterogeneity disappears. More importantly, the prey and predator densities exhibit opposite trends: The prey density increases monotonically with η, whereas the predator density decreases. This provides direct numerical evidence for the predator release mechanism. The environmental stress suppresses the predator population more strongly, which weakens predation pressure and thereby indirectly favors the prey.

The bifurcation diagram therefore shows that environmental stress has a twofold effect. On the one hand, it changes the stability regime of the system: It first stabilizes the local reaction kinetics and then suppresses diffusion-driven spatial instability. On the other hand, it alters the community structure in the stable homogeneous regime. Although the stress acts negatively on both populations, the predator is more strongly suppressed, and the prey benefits indirectly from the reduced predation pressure. This explains the observed predator release effect and clarifies why the prey's equilibrium density can increase under moderate environmental stress.

To further describe the delay-induced temporal instability, in Figure 8, we plot the critical Hopf bifurcation delay $\tau_*(\eta)$ and the prey equilibrium density $u_*(\eta)$ as functions of the environmental stress η, with $\chi = 2.0$. For each fixed value of η, the mode-dependent Hopf threshold associated with the k-th Neumann mode is denoted $\tau_k^*(\eta)$. The critical delay shown in Figure 8 is computed as the lower envelope

$$\tau_*(\eta) = \min_{1 \le k \le k_{\max}} \tau_k^*(\eta), \tag{6.2}$$

and the corresponding dominant unstable mode is defined by

$$k_{\mathrm{dom}}(\eta) = \arg\min_{1 \le k \le k_{\max}} \tau_k^*(\eta). \tag{6.3}$$

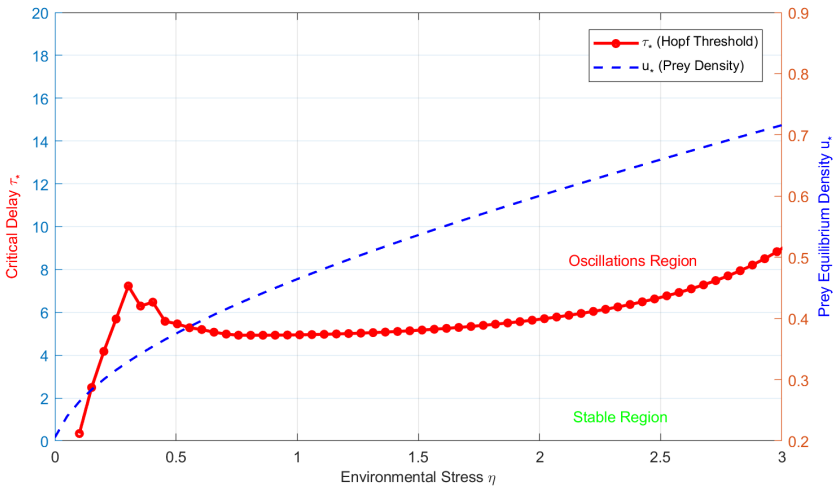

Figure 8. Effect of environmental stress η on the critical Hopf bifurcation delay $\tau_*(\eta)$ (red solid line) and the prey equilibrium density $u_*(\eta)$ (blue dashed line) at $\chi = 2.0$. The critical delay is obtained as the lower envelope of the mode-dependent Hopf thresholds $\tau_k^*(\eta)$. The nonmonotone profile of $\tau_*(\eta)$ reflects the competition among different spatial Hopf modes.

To make the mode-switching mechanism explicit, we further plot $k_{\mathrm{dom}}(\eta)$ in Figure 9. The stepwise variation of k_{dom} shows that the first unstable Hopf mode changes as the environmental stress varies. Hence, the irregular or nonsmooth parts of $\tau_*(\eta)$ in Figure 8 are not numerical artifacts but are caused by the switching of the minimizing branch within the family $\{\tau_k^*(\eta)\}_{k\geq 1}$.

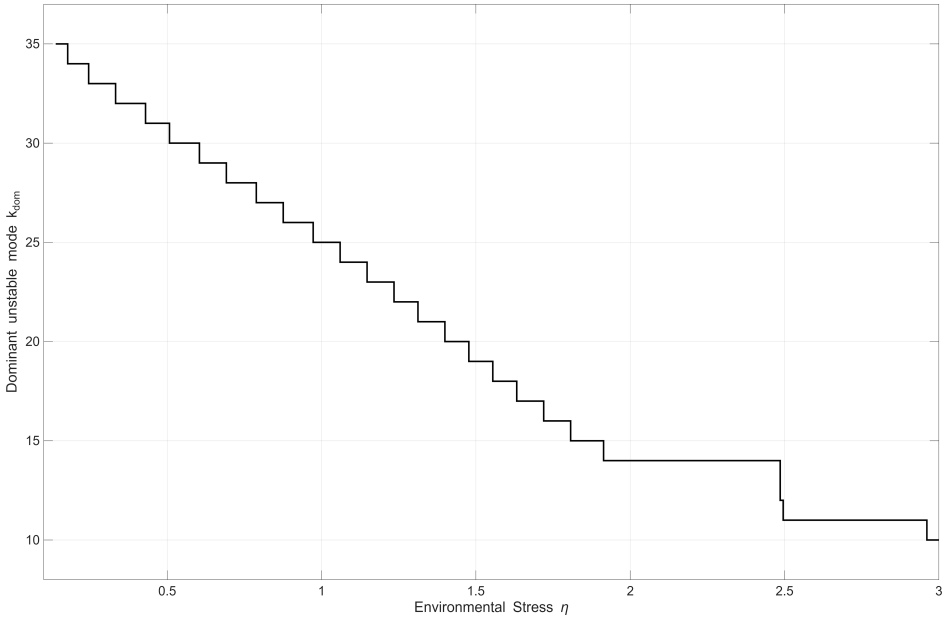

Figure 9. Dominant unstable Hopf mode $k_{\mathrm{dom}}(\eta)$ as a function of the environmental stress η at $\chi = 2.0$. For each η, k_{dom} is defined by (6.3). The stepwise changes indicate that different spatial modes become dominant in different stress regimes, providing direct evidence of mode switching.

For completeness, Figure 10 displays several mode-dependent Hopf thresholds together with their lower envelope. This figure confirms that $\tau_*(\eta)$ is formed by different branches $\tau_k^*(\eta)$. The crossing and exchange of these branches explain the mode-jumping phenomenon observed in Figure 9.

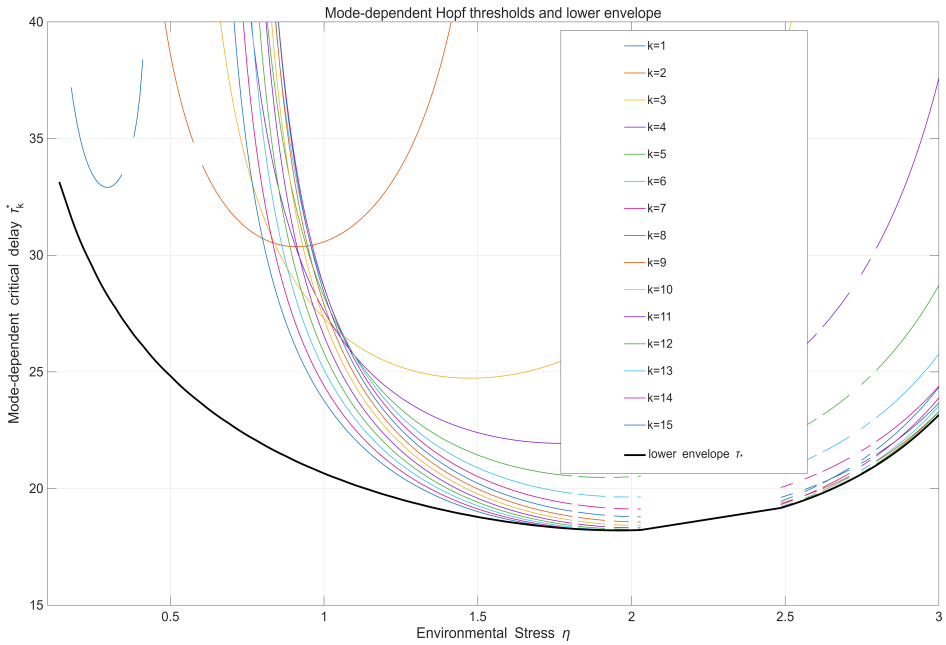

Figure 10. Mode-dependent Hopf thresholds $\tau_k^*(\eta)$ and their lower envelope $\tau_*(\eta)$. The colored curves correspond to different spatial modes k, while the black solid curve represents the minimum over all computed modes. The exchange of the minimizing branch gives rise to the observed mode-jumping phenomenon.

The prey equilibrium density $u_*(\eta)$ increases monotonically in Figure 8, which is consistent with the predator release mechanism discussed above. As the environmental stress suppresses the predator more strongly, the predation pressure on the prey is weakened, and the prey equilibrium density consequently increases.

The critical delay $\tau_*(\eta)$, however, exhibits a nonmonotone profile. For relatively small and intermediate stress levels, the lower envelope $\tau_*(\eta)$ is controlled by different spatial modes. In this regime, small changes in η may change the minimizing mode $k_{\mathrm{dom}}(\eta)$, leading to visible changes in the slope and local shape of the critical delay curve. This is the mode-jumping mechanism: The Hopf instability is still delay-induced, but the spatial mode that first loses stability is not fixed.

For larger stress levels, the critical delay varies more smoothly. In this parameter range, the predator density is reduced and the effective trophic interaction becomes weaker. As a result, the delayed feedback has to be stronger (or, equivalently, the delay has to be larger) before temporal oscillations are triggered. Thus, environmental stress may raise the Hopf threshold after the system has moved into a prey-dominated coexistence regime. This stabilizing effect should be understood in this restricted sense: It increases the delay threshold for the coexistence state under the present parameter setting, while at the same time altering the community structure towards higher prey density and lower predator abundance.

Overall, Figures 8 to 10 show that environmental stress affects temporal stability through two coupled mechanisms. First, it changes the coexistence equilibrium and weakens predator-mediated feedback. Second, it changes the spatial mode that realizes the minimal Hopf threshold. The observed nonmonotonicity of $\tau_*(\eta)$ is therefore a consequence of both equilibrium displacement and mode competition.

7. Conclusions

In this paper, we proposed and analyzed a diffusive predator–prey model incorporating memory-based prey-taxis and external environmental stress. Our main objective was to understand how these internal cognitive mechanisms and external pressures jointly shape spatiotemporal pattern formation and ecosystem stability. The main findings are summarized as follows.

First, we established the global well-posedness of the system and derived threshold conditions for the existence of equilibria. We identified the critical threshold χ_c for Turing bifurcation and the critical delay τ_* for Hopf bifurcation, pinpointing a codimension-2 bifurcation point where spatial and temporal instabilities interact.

Second, our analysis highlights a dual stabilizing role of memory-based prey-taxis. Contrary to the traditional view that taxis acts solely as a destabilizing force, our results show that sufficiently strong attractive prey-taxis ($\chi > \chi_c$) suppresses diffusion-driven Turing patterns. The results indicate that prey-taxis has distinct effects on spatial and temporal instabilities. A sufficiently large taxis sensitivity can suppress diffusion-driven Turing patterns and drive the system toward spatial homogeneity. Nevertheless, when the taxis response is delayed, increasing χ may lower the Hopf threshold $\tau_*(\chi)$, so that oscillations arise for smaller delays. Hence, the role of memory-based prey-taxis is not purely stabilizing; rather, it creates a trade-off between the suppression of stationary spatial patterns and the enhancement of delay-induced temporal instability.

Third, the introduction of environmental stress η leads to an interesting predator release effect. Moderate stress disproportionately impacts the predator population, indirectly allowing the prey density to increase. Furthermore, environmental stress acts as a critical bifurcation parameter, driving the system from ODE instability to Turing instability and ultimately to a stable homogeneous state. The nonmonotonic behavior of the critical delay τ_* during this transition implies a mode-jumping phenomenon, reflecting the competition between different spatial modes under stress.

Finally, our numerical simulations confirmed the existence of four distinct dynamic regions: Stable homogeneous states, stationary Turing patterns, spatially nonhomogeneous periodic solutions, and complex spatiotemporal dynamics arising from Turing–Hopf interactions.

Author contributions

Dazhuo Liu: Conceptualization, methodology, formal analysis, writing-original draft, writing-review and editing, supervision, and funding acquisition. Xuewen Tan: Methodology, validation, numerical simulations, visualization, and writing-review and editing. All authors have read and approved the final version of the manuscript.

Use of Generative-AI tools declaration

The authors used ChatGPT to assist with language polishing, grammar checking, and minor wording improvement during the preparation of this manuscript. The authors reviewed and edited all AI-assisted outputs and take full responsibility for the content of the published article.

Acknowledgments

Fujian Province Education Science Planning Special Project for High Quality Development of Basic Education - The Era's Demands and Implementation Strategies for Empowering High Quality Development of Mathematics Education with Mathematical Culture (FJJKWT24-017).

Conflict of interest

The authors declare that they have no conflict of interest.

References

1. P. A. Abrams, The evolution of predator–prey interactions: Theory and evidence, *Annu. Rev. Ecol. Syst.*, **31** (2000), 79–105. https://doi.org/10.1146/annurev.ecolsys.31.1.79
2. F. Yi, J. Wei, J. Shi, Bifurcation and spatiotemporal patterns in a homogeneous diffusive predator–prey system, *J. Differ. Equ.*, **246** (2009), 1944–1977. https://doi.org/10.1016/j.jde.2008.10.024
3. X. Cao, W. Jiang, Turing–Hopf bifurcation and spatiotemporal patterns in a diffusive predator–prey system with Crowley–Martin functional response, *Nonlinear Anal. Real World Appl.*, **43** (2018), 428–450. https://doi.org/10.1016/j.nonrwa.2018.03.010
4. W. Jiang, X. Cao, C. Wang, Turing instability and pattern formations for reaction-diffusion systems on 2D bounded domain, *Discrete Contin. Dyn. Syst. Ser. B*, **27** (2022), 1163. https://doi.org/10.3934/dcdsb.2021085
5. Y. Song, X. Tang, Stability, steady-state bifurcations, and Turing patterns in a predator–prey model with herd behavior and prey-taxis, *Stud. Appl. Math.*, **139** (2017), 371–404. https://doi.org/10.1111/sapm.12165
6. J. S. Guo, M. Shimojo, Spatio-temporal oscillation for a singular predator–prey model, *J. Math. Anal. Appl.*, **459** (2018), 1–9. https://doi.org/10.1016/j.jmaa.2017.10.080
7. R. Zhang, X. Ren, Lyapunov functions for some epidemic model with high risk and vaccinated class, *Appl. Math. Lett.*, **163** (2025), 109437. https://doi.org/10.1016/j.aml.2024.109437
8. X. Zhang, Q. An, H. Wang, Global solvability and stability of cognitive consumer-resource model with nonlocal usage of memory, *J. Math. Anal. Appl.*, **556** (2026), 130076. https://doi.org/10.1016/j.jmaa.2025.130076
9. X. Zhang, S. Li, Y. Yuan, Q. An, Effect of discontinuous harvesting on a diffusive predator–prey model, *Nonlinearity*, **37** (2024), 115016. https://doi.org/10.1088/1361-6544/ad7fc3
10. J. G. Wang, X. Y. Meng, X. Lei, Bifurcations and control of plant–herbivore systems with spatiotemporal nonlocal effects in arid regions, *Int. J. Bifurcat. Chaos*, (2026), 2650071. https://doi.org/10.1142/S0218127426500719
11. H. Y. Jin, Z. A. Wang, Global stability of prey-taxis systems, *J. Differ. Equ.*, **262** (2017), 1257–1290. https://doi.org/10.1016/j.jde.2016.10.010
12. S. Wu, J. Shi, B. Wu, Global existence of solutions and uniform persistence of a diffusive predator–prey model with prey-taxis, *J. Differ. Equ.*, **260** (2016), 5847–5874. https://doi.org/10.1016/j.jde.2015.12.024

13. X. Liu, T. Zhang, X. Meng, T. Zhang, Turing–Hopf bifurcations in a predator–prey model with herd behavior, quadratic mortality and prey-taxis, *Physica A*, **496** (2018), 446–460. https://doi.org/10.1016/j.physa.2018.01.006
14. X. Zhang, B. Wu, Dynamics of a diffusion-advection model with local perception of toxins, *Chaos Soliton. Fract.*, **201** (2025), 117259. https://doi.org/10.1016/j.chaos.2025.117259
15. P. Wu, C. Fang, Spatiotemporal dynamics of syphilis in Xinjiang via a demographic-geographic data-validated reaction diffusion model, *J. Math. Phys.*, **66** (2025). https://doi.org/10.1063/5.0273893
16. X. Y. Meng, Z. W. Liang, Dynamics analysis of a delayed diffusive predator–prey model with memory-based diffusion and fear effect of prey, *Int. J. Biomath.*, (2025), 2550101. https://doi.org/10.1142/S1793524525501013
17. H. Wang, Y. Salmaniw, Open problems in PDE models for knowledge-based animal movement via nonlocal perception and cognitive mapping, *J. Math. Biol.*, **86** (2023), 71. https://doi.org/10.1007/s00285-023-01905-9
18. J. R. Potts, M. A. Lewis, Spatial Memory and Taxis-Driven Pattern Formation in Model Ecosystems, *Bull. Math. Biol.*, **81** (2019), 2725–2747. https://doi.org/10.1007/s11538-019-00626-9
19. J. Shi, C. Wang, H. Wang, X. Yan, Diffusive spatial movement with memory, *J. Dyn. Differ. Equ.*, **32** (2019), 979–1002. https://doi.org/10.1007/s10884-019-09757-y
20. J. Shi, C. Wang, H. Wang, Spatial movement with distributed memory, *J. Math. Biol.*, **82** (2021), 33. https://doi.org/10.1007/s00285-021-01588-0
21. Y. Song, Y. Peng, T. Zhang, The spatially inhomogeneous Hopf bifurcation induced by memory delay in a memory-based diffusion system, *J. Differ. Equ.*, **300** (2021), 597–624. https://doi.org/10.1016/j.jde.2021.08.010
22. Y. Song, J. Shi, H. Wang, Spatiotemporal dynamics of a diffusive consumer-resource model with explicit spatial memory, *Stud. Appl. Math.*, **148** (2022), 373–395. https://doi.org/10.1111/sapm.12443
23. X. Y. Meng, L. Xiao, Hopf bifurcation and Turing instability of a delayed diffusive zooplankton–phytoplankton model with hunting cooperation, *Int. J. Bifurcat. Chaos*, **34** (2024), 2450090. https://doi.org/10.1142/S0218127424500901
24. H. Freedman, J. Shukla, Models for the effect of toxicant in single-species and predator–prey systems, *J. Math. Biol.*, **30** (1991), 15–30. https://doi.org/10.1007/BF00168004
25. Q. Huang, H. Wang, M. A. Lewis, The impact of environmental toxins on predator–prey dynamics, *J. Theor. Biol.*, **378** (2015), 12–30. https://doi.org/10.1016/j.jtbi.2015.04.019
26. D. R. Thommandru, S. Kundu, Uncovering ecological thresholds: stress-driven response, time delay, and intraspecies competition among predators in predator–prey dynamics, *Nonlinear Dyn.*, (2025), 1–24. https://doi.org/10.1007/s11071-025-11790-0
27. C. Shan, Q. Huang, Direct and indirect effects of toxins on competition dynamics of species in an aquatic environment, *J. Math. Biol.*, **78** (2019), 739–766. https://doi.org/10.1007/s00285-018-1290-2
28. P. Zhou, Q. Huang, A spatiotemporal model for the effects of toxicants on populations in a polluted river, *SIAM J. Appl. Math.*, **82** (2022), 95–118. https://doi.org/10.1137/21M1405629

29. J. Xing, Q. Huang, H. Nie, Dynamical analysis of a diffusive population-toxicant model with toxicant-taxis in polluted aquatic environments, *Math. Biosci.*, **372** (2024), 109193. https://doi.org/10.1016/j.mbs.2024.109193
30. Y. Wang, J. Shi, J. Wang, Persistence and extinction of population in reaction–diffusion–advection model with strong Allee effect growth, *J. Math. Biol.*, **78** (2019), 2093–2140. https://doi.org/10.1007/s00285-019-01334-7
31. C. Zhang, H. Yuan, Pattern formation in a variable diffusion predator–prey model with additive Allee effect, *Math. Methods Appl. Sci.*, **43** (2020), 4023–4035. https://doi.org/10.1002/mma.6171
32. A. Chattopadhyay, S. Banerjee, A. Samadder, S. Bhattacharya, Is toxicity a curse or blessing, or both?—searching answer from a disease-induced consumer-resource system, *Ecol. Model.*, **486** (2023), 110534. https://doi.org/10.1016/j.ecolmodel.2023.110534
33. A. Lunardi, *Analytic semigroups and optimal regularity in parabolic problems*, Springer Science & Business Media, 2012.
34. M. Winkler, Aggregation vs. global diffusive behavior in the higher-dimensional Keller–Segel model, *J. Differ. Equ.*, **248** (2010), 2889–2905. https://doi.org/10.1016/j.jde.2010.02.008
35. D. Horstmann, M. Winkler, Boundedness vs. blow-up in a chemotaxis system, *J. Differ. Equ.*, **215** (2005), 52–107. https://doi.org/10.1016/j.jde.2004.10.022
36. T. Faria, Normal forms and Hopf bifurcation for partial differential equations with delays, *Trans. Amer. Math. Soc.*, **352** (2000), 2217–2238. https://doi.org/10.1090/S0002-9947-00-02280-7

AIMS Press